ELSEVIER

Journal of Nuclear Materials 252 (1998) 235–256

journal of nuclear materials

Low volatile fission-product release and fuel volatilization during severe reactor accident conditions

B.J. Lewis [a,*], B.J. Corse [a], W.T. Thompson [a], M.H. Kaye [a], F.C. Iglesias [b], P. Elder [c,1], R. Dickson [c], Z. Liu [c]

[a] *Department of Chemistry and Chemical Engineering, Royal Military College of Canada, Kingston, Ont., Canada K7K 7B4*
[b] *Ontario Hydro, Reactor Safety and Operational Analysis Department, 700 University Avenue, Toronto, Ont., Canada M5G 1X6*
[c] *Atomic Energy of Canada Limited-Research Company, Chalk River Laboratories, Chalk River, Ont., Canada K0J 1J0*

Received 30 April 1997; accepted 26 September 1997

Abstract

An analytical model has been developed to describe the release behavior of low-volatile fission products from uranium dioxide fuel under severe reactor accident conditions. The effect of the oxygen potential on the chemical form and volatility of fission products is determined by Gibbs-energy minimization. The release kinetics are calculated according to the rate-controlling step of diffusional transport in the fuel matrix or fission product vaporization from the fuel surface. The effect of fuel volatilization (i.e., matrix stripping) on the release behavior is also considered. The model has been validated against several out-of-pile annealing experiments performed at high temperature in various oxidizing and reducing conditions. © 1998 Elsevier Science B.V.

1. Introduction

During a severe reactor accident, fission products (FPs) will be released from the degraded core. The release behavior will depend on the various physical and chemical processes that occur in the fuel matrix and in the surrounding gaseous atmosphere. The release kinetics of the more volatile FPs (e.g., Xe, Kr, Cs and I) have been shown to depend on a rate-limiting process of solid-state diffusion through the UO_2 fuel matrix [1,2]. On the other hand, the release of the low-volatile FPs will more likely depend on the partial pressures of the various chemical forms of the FP (e.g., metal, oxide, hydroxide, mixed oxide, etc.) [3–7]. The FP speciation will be influenced by the oxygen potential of the gas environment, which can change as a result of hydrogen production from steam oxidation of the structural materials (i.e., zircaloy) within the damaged core, the relative quantities of fuel to gas at the site of the reaction, temperature and total hydrostatic pressure.

An additional mechanism of release results from the volatilization of the fuel matrix itself as the UO_{2+x} oxidizes to the more volatile UO_3 phase. Fission products that were previously contained in the volatilized portion of the matrix will be immediately released if they have a high partial pressure, whereas the low-volatile ones will condense and become concentrated at the underlying fuel surface. The fuel volatilization therefore results in a 'matrix stripping' process of release in place of matrix diffusion [8–10]. For these low-volatile products, the subsequent release will again be dictated by vaporization from the fuel surface.

In this work, an analytical model is developed to describe the low-volatile fission-product release behavior and fuel volatilization kinetics in accordance with equilibrium thermodynamics and mass transfer considerations [4]. Chemical equilibrium is assumed for the determination of the FP chemical form and partial pressure using a Gibbs-energy minimization technique based on the Facility for the Analysis of Chemical Thermodynamics (FACT) [11].

* Corresponding author. Tel.: +1-613 541 6611; fax: +1-613 542 9489; e-mail: lewis_b@rmc.ca.
[1] Present address: Atomic Energy Control Board, P.O. Box 1046, Station B, Ottawa, Canada K1P 5S9.

0022-3115/98/$19.00 © 1998 Elsevier Science B.V. All rights reserved.
PII S0022-3115(97)00292-4

The FACT database [12–15] has been supplemented with additional thermodynamic data on 150 chemical species following an extensive literature review [5–7,16–21]. This treatment is much more extensive than earlier work since both CANDU and pressurized water reactor (PWR) fuel types are considered over a wide range of accident conditions of temperature and oxygen potential; in addition, previous thermodynamic calculations ignored the possibility of a compound containing more than one metal [5–7]. A closed-form algorithm, based on a method of chemical potentials, is also developed to rapidly re-construct all partial compound pressures for the vaporization calculation.

The model has been compared to measured data obtained in several high-temperature annealing experiments, conducted in both reducing and oxidizing conditions. These measured results include earlier published data for tests with Zircaloy-clad fuel specimens from spent PWR fuel rods at the Commissariat à l'Energie Atomique [4,22], and new data from a separate-effects experiment at the Chalk River Laboratories using a fuel fragment from a spent CANDU fuel rod.

2. Model development

The release of fission products from the damaged fuel rod occurs as a multi-step process, consisting of: (i) transport through the fuel matrix and/or release due to volatilization of the fuel matrix, and (ii) fission-product vaporization into the gas stream flowing past the rod. The release kinetics are therefore controlled by the rate-limiting step. These mechanisms are described mathematically in the following sections.

2.1. Fission-product transport through the fuel matrix

Fission-product transport in the uranium dioxide fuel matrix can be described by a generalized diffusional release process. The release fraction is given by

$$F_{\mathrm{d}} = \frac{N_{\mathrm{d}}(\tau)}{N_{\mathrm{go}}}, \tag{1}$$

where $N_{\mathrm{d}}(\tau)$ is the number of atoms which have diffused through the solid matrix and N_{go} is the original inventory in the fuel at time $t = 0$. The function $F_{\mathrm{d}}(\tau)$ is given by a transformed Booth relation [2,4],

$$F_{\mathrm{d}} = \begin{cases} 6\sqrt{\tau/\pi} - 3\tau, & \text{for } \tau \le 0.1, \\ 1 - \left(6/\pi^2\right)\exp\{-\pi^2\tau\}, & \text{for } \tau > 0.1. \end{cases} \tag{2}$$

The dimensionless variable τ is evaluated from the integral relation

$$\tau = \int_0^t D'(t)\,\mathrm{d}t, \tag{3}$$

where $D' = D/a^2$, D is the diffusion coefficient (in m^2/s) and a is the grain radius (in m). Eq. (3) accounts for a time-variable diffusivity that depends directly on the temperature T and on the stoichiometry deviation x in UO_{2+x} as the fuel is oxidized. The Booth model implicitly assumes that the controlling process in fission product release is lattice diffusion through a collection of 'equivalent' grain spheres. The subsequent migration of the fission product from the grain boundaries to the free surfaces of the fuel specimen is assumed to occur without delay. This approach is reasonable since gaseous diffusion coefficients are so much larger than solid-state diffusivities that transport in the existing open porosity of high burnup fuel could not be rate limiting. In addition, release by grain boundary sweeping is not an important release mechanism because the grain growth is limited by the pinning of the grain boundaries by the fission-product bubbles.

The diffusion coefficient for the volatile cesium species is given by the composite expression [2,23]

$$D(x, T) = \left[1 + F_{\mathrm{in}}\frac{\mathrm{d}T}{\mathrm{d}t}\right] D_{\mathrm{in}} \exp\left\{-\frac{Q_{\mathrm{in}}}{RT}\right\} + x^2 D_{\mathrm{ox}} \exp\left\{-\frac{Q_{\mathrm{ox}}}{RT}\right\}. \tag{4}$$

The parameters in Eq. (4) for the two different fuel types are listed in Table 1. In the Booth representation, the diffusivity in Eq. (4) is an 'effective' quantity, incorporating lattice diffusion, trapping and any delay in the tunnel interlinkage. In particular, the first term in Eq. (4) accounts for intrinsic diffusion, including any augmented release during temperature ramps as a consequence of fuel cracking, bubble precipitation and release, whereas the second term describes accelerated diffusion from fuel-matrix oxidation due to enhanced uranium vacancy production.

Equivalently, Eqs. (2)–(4) could be replaced by a more sophisticated treatment as used, for example, in the Victoria code of Ref. [21] to account for extra-granular transport in the fuel porosity. Alternatively, the more complicated model of Ref. [24] could be employed which accounts for both diffusion and bubble trapping effects during annealing where the fission-product transport is described by a series of coupled reaction rate equations. However, fuel-oxidative effects have been ignored in this latter model, and diffusion has been treated as a simple first-order rate process in order to provide a more tractable solution. Thus, the present model has been adopted since it contains the underlying physical phenomena, but is not as computationally intensive.

For the evaluation of the diffusivity in Eq. (4), the fuel oxidation kinetics must be determined. The stoichiometry deviation x can be evaluated as a function of time according to [2]

$$\frac{\mathrm{d}x}{\mathrm{d}t} = -\alpha(S/V)\left[x - x_{\mathrm{e}}(t)\right], \tag{5}$$

Table 1
Parameters for diffusion coefficient

Fuel type	Intrinsic diffusion			Vacancy-enhanced diffusion	
	temperature ramp factor, F_{in} (s/K)	pre-exponential factor, D_{in} (m^2/s)	activation energy, Q_{in} (cal/mol)	pre-exponential factor, D_{ox} (m^2/s)	activation energy, Q_{ox} (cal/mol)
PWR[a]	0	1.35×10^{-8} [b]	79 700	2.22×10^{-8}	40 200
CANDU[a]	178[c]	7.6×10^{-10}	70 000	2.22×10^{-8}	40 200

[a] Taken from Ref. [2].
[b] The pre-exponential factor incorporates the temperature ramp effect.
[c] Based on the analysis in Ref. [23].

where $\alpha = 0.365 \exp\{-23\,500/T\}$ (m/s) and S/V is the effective surface-to-volume ratio of the fuel (m^{-1}). This effective ratio is equal to ~ 3 times the geometrical one in order to account for surface roughness and microcracking of the fuel [2]. The equilibrium stoichiometry deviation, x_e, in Eq. (5) can be evaluated by equating the oxygen potential in the fuel to that in the atmosphere. The oxygen potential (in kJ/mol O_2) for hyperstoichiometric fuel (UO_{2+x}) can be calculated from the Blackburn thermochemical model [25],

$$\Delta G_{O_2} = RT \ln(p_{O_2}) = RT \ln\left\{\left(\frac{x(2+x)}{1-x}\right)^2 k\right\}, \qquad (6)$$

where $\ln k = 108\,x^2 - 32\,700/T + 9.92$, R is the ideal gas constant ($= 8.314 \times 10^{-3}$ kJ mol^{-1} K^{-1}), T is the temperature (in K) and p_{O_2} is the oxygen partial pressure (in atm). Eq. (6) is only strictly valid for pure UO_2 (i.e., at zero burnup) and neglects the effect of any dissolved fission products in the lattice. The oxygen potential for an ideal gas mixture in the atmosphere consisting of H_2O, H_2 (produced from the Zircaloy/steam reaction), O_2 and inert gas (due to the possible presence of air in the reactor vessel or channel) can be evaluated as [26,27]

$$\frac{p_i}{p_{tot}} = \frac{\dot{n}_i}{\sum_{j=1}^{N} \dot{n}_j}, \qquad (7)$$

where p_i is the partial pressure of component i, p_{tot} is the total pressure of all gases (atm), $\dot{n}_i$ is the instantaneous molar flow rate of component i, and N is the total number of component gases in the system. For the H_2O decomposition reaction

$$H_2O \overset{K_{H_2O}}{\Leftrightarrow} H_2 + \tfrac{1}{2}O_2, \qquad (8)$$

the equilibrium constant, K_{H_2O}, is [28]

$$K_{H_2O} = \frac{p_{H_2}\sqrt{p_{O_2}}}{p_{H_2O}} = \exp\left\{0.9794 \ln T - 1.1125 - \frac{28\,820}{T}\right\}. \qquad (9)$$

If the rate of H_2O dissociation required to maintain equilibrium is β, the molar flow rates after dissociation are [26]

$$\dot{n}_{H_2O} = \dot{n}^0_{H_2O} - \beta, \qquad \dot{n}_{H_2} = \dot{n}^0_{H_2} + \beta,$$
$$\dot{n}_{O_2} = \dot{n}^0_{O_2} + \frac{\beta}{2}, \qquad (10)$$

where the superscript '0' refers to the initial input gas quantities. Hence, the conditions for equilibrium can be described by combining Eqs. (7), (9) and (10),

$$K_{H_2O} = \frac{\dot{n}^0_{H_2} + \beta}{\dot{n}^0_{H_2O} - \beta} \times \sqrt{\frac{p_{tot}\left\{\dot{n}^0_{O_2} + \frac{1}{2}\beta\right\}}{\dot{n}^0_{H_2O} + \dot{n}^0_{H_2} + \dot{n}^0_{O_2} + \dot{n}^0_{inert} + \frac{1}{2}\beta}}. \qquad (11)$$

Eq. (11) can be solved for β, and knowing the input molar flows, the partial pressures of the individual components are determined as follows:

$$\frac{p_{H_2}}{p_{tot}} = \frac{\dot{n}^0_{H_2} + \beta}{\sum_{j=1}^{N} n_j}, \qquad \frac{p_{O_2}}{p_{tot}} = \frac{\dot{n}^0_{O_2} + \frac{1}{2}\beta}{\sum_{j=1}^{N} n_j},$$
$$\frac{p_{H_2O}}{p_{tot}} = \frac{\dot{n}^0_{H_2O} - \beta}{\sum_{j=1}^{N} n_j}, \qquad \frac{p_{inert}}{p_{tot}} = \frac{\dot{n}^0_{inert}}{\sum_{j=1}^{N} n_j}, \qquad (12)$$

where $\sum_{j=1}^{N} n_j = \dot{n}^0_{H_2O} + \dot{n}^0_{H_2} + \dot{n}^0_{O_2} + \dot{n}^0_{inert} + \frac{1}{2}\beta$. This methodology can also be developed further to include the measurement of the oxygen content of the flowing gas mixture with the use of solid-state oxygen sensors at upstream and downstream locations of the fuel specimen (see appendix A of Ref. [26]).

Thus, equating the oxygen partial pressures in Eqs. (6) and (12), one can obtain x_e as a function of time for variable atmospheric conditions (i.e., a changing H_2/H_2O ratio). The H_2/H_2O ratio will change with time as a consequence of hydrogen production from cladding and fuel oxidation. In turn, $x(t)$ can be evaluated with Eq. (5) for use in the diffusion coefficient of Eq. (4).

2.2. Fission-product release from fuel volatilization

As discussed in Section 1, fission-product release from the fuel matrix can also arise from a matrix-stripping process as a consequence of fuel volatilization. Fuel volatilization in oxidizing conditions can be described by the following reaction [10]:

$$UO_{2+x}(s) + \tfrac{1}{2}(1-x)O_2 \leftrightarrow UO_3(g). \tag{13}$$

The equilibrium partial pressure of UO_3 for the above reaction will depend on the exposure time [10],

$$p_{UO_3}(t) = p_{O_2}^{[1-x(t)]/2} \exp\left\{ -\frac{\Delta G_{(13)}(t)}{RT} \right\}, \tag{14}$$

where

$$\Delta G_{(13)}(t) = \Delta G_f^0(UO_3(g)) - \Delta G_f^0(UO_2) - \tfrac{1}{2}\int_0^{x(t)} \Delta G_{O_2}\, dx. \tag{15}$$

Eq. (14) is conservative since it implicitly assumes that the equilibrium in Eq. (13) has been reached for a given value of $x(t)$ as determined by the kinetics of Eq. (5). The partial molar Gibbs energy of oxygen in UO_{2+x} can be integrated using the Blackburn thermochemical model in Eq. (6) such that

$$\tfrac{1}{2}\int_0^x \Delta G_{O_2}\, dx = RT\left\{ \ln\left(\frac{x^x(2+x)^{2+x}(1-x)^{1-x}}{4} \right) - \frac{x}{2}\left(\frac{32\,700}{T} - 7.92 \right) + 18x^3 \right\}. \tag{16}$$

In addition, the UO_2 and UO_3 formation energies (in kJ mol^{-1}) in Eq. (15) are given by [29,30]

$$\Delta G_f^0(UO_3(g)) - \Delta G_f^0(UO_2) = 253.33 - 0.09523T. \tag{17}$$

For the evaluation of Eq. (14), the oxygen partial pressure and instantaneous stoichiometry deviation $x(t)$ is determined in accordance with the analysis of Section 2.1. This treatment for the prediction of the partial UO_3 pressure, however, neglects the presence of the fission product dissolved in the fuel at the solid–gas interface.

The rate of volatilization of the fuel matrix is controlled by UO_3 mass transport through a boundary layer at the surface of the fuel. Thus, the fuel volatilization rate depends on the difference between the UO_3 partial pressure at the solid–gas interface and in the bulk gas, and the mass transfer from the fuel surface into the carrier gas stream. From mass transfer theory, the volatilization rate R_{vol} (in molecule s^{-1}) from an exposed surface area S (m^2) is given by [3,4,10,31]

$$R_{vol} = \frac{SN_A}{M_{UO_{2+x}}}\frac{dm}{dt} = SN_A k_m\left(\frac{p_{UO_3}^s}{p_{tot}} - \frac{p_{UO_3}^\infty}{p_{tot}} \right), \tag{18}$$

where N_A is Avogadro's number ($= 6.022 \times 10^{23}$ molecule mol^{-1}), $M_{UO_{2+x}}$ is the molecular weight of UO_{2+x} (kg mol^{-1}), dm/dt is the vaporization mass flux of UO_{2+x} (kg m^{-2} s^{-1}), k_m is the mass transfer coefficient (mol m^{-2} s^{-1}) (see Section 2.3.1), $p_{UO_3}^s$ is the equilibrium partial pressure of UO_3 at the fuel surface (Eq. (14)) and $p_{UO_3}^\infty$ is the UO_3 partial pressure in the bulk gas stream which is conservatively assumed to be negligible in the present analysis, i.e., this partial pressure would be negligible for the small fuel samples.

In the matrix stripping process, the fission product release from the volatized fuel matrix will concentrate on the underlying fuel surface (for eventual vaporization). The fraction of fission products released from the fuel matrix can be equated to the mass fraction of volatilized fuel material (F_{vol}), such that

$$F_{vol} = \frac{\Delta m}{m_0}, \tag{19}$$

where m_0 is the initial mass of fuel (in kg) and Δm is the mass of volatilized UO_{2+x},

$$\Delta m = \frac{M_{UO_{2+x}}}{N_A}\int_0^t R_{vol}\, dt. \tag{20}$$

In this calculation it is implicitly assumed that a constant fission-product distribution exists within the fuel, i.e., pellet rim effects that develop, for example, in high-burnup fuel are ignored.

The fission products released by matrix stripping are no longer available for diffusional transport in the fuel matrix. Hence, using Eqs. (1) and (19), mass conservation implies that the number of atoms which reach the fuel surface by either diffusion or matrix stripping (N_{fs}) are

$$N_{fs} = \{(1 - F_{vol})F_d + F_{vol}\}N_{go}. \tag{21}$$

Equivalently, the combined release fraction (F_{fs}) for the two release processes from the matrix to the fuel surface is

$$F_{fs} = \frac{N_{fs}}{N_{go}} = \{(1 - F_{vol})F_d + F_{vol}\}. \tag{22}$$

The fission products that have reached the fuel surface (N_{fs}) are concentrated at this surface and must be subsequently vaporized for any release to occur (see Section 2.3).

2.3. Fission-product vaporization

The vaporization release of low-volatile fission products from the fuel depends on the partial pressure of the species and the mass transfer from the fuel surface into the carrier gas stream. Analogous to Eq. (18), the release rate (R_{iv}) (in atom/s) of a fission product species i, vaporized from an exposed fuel surface area S (in m^2) is

$$R_{iv} = S\gamma_i N_A k_{im}(x_{is} - x_{i\infty}), \tag{23}$$

where k_{im} is the mass transfer coefficient (see Section 2.3.1) (mol m^{-2} s^{-1}), x_{is} is the mole fraction of fission product i at the surface of the fuel, $x_{i\infty}$ is the mole fraction of fission product i in the bulk gas stream, γ_i is the number of atoms per molecule of fission product i and N_A is Avogadro's number ($= 6.022 \times 10^{23}$ mol^{-1}).

The mole fraction of fission product at the surface of the fuel is

$$x_{is} = \frac{p_{iv}}{p_{tot}}, \tag{24}$$

where p_{iv} is the partial pressure (in atm) of the fission product i in the vapor phase (see Section 2.3.2), and p_{tot} is the total system pressure. For the small quantities of low-volatile fission products anticipated in the bulk stream, it can again be assumed that $x_{i\infty} \approx 0$.

The number of atoms of a given fission product which are released by vaporization from the fuel surface (N_r) is given by

$$N_r = \int_0^t R_{iv}(t)\,dt, \tag{25}$$

thereby yielding a release fraction for vaporization (F_v) of

$$F_v = \frac{N_r}{N_{go}} = \frac{\int_0^t R_{iv}(t)\,dt}{N_{go}}. \tag{26}$$

Finally, the overall release fraction (F) for a given fission product is taken as the smaller of the two release fractions for release to the fuel surface (F_{fs}) (Eq. (22)) versus vaporization from that surface (F_v) (Eq. (26)) [4],

$$F = \min(F_{fs}, F_v). \tag{27}$$

The smaller fractional release value indicates the rate-controlling step [4].

If the fuel is surrounded by a Zircaloy cladding, some fission products can be chemically-trapped in the cladding until it becomes oxidized. For example, tellurium will be released when the clad is $\sim 60\%$ oxidized, while antimony will remain trapped until the oxidation process is complete [4]. The effect of fission-product trapping for these species can be empirically modelled as a reduced overall fractional release where the result of Eq. (27) is multiplied by the fraction $(1 - \zeta)$. Here ζ is a trapping fraction which can be correlated with the oxidation state of the cladding and the temperature as shown in Ref. [4].

2.3.1. Mass transfer coefficient

The mass transfer coefficient can be evaluated for a given geometry based on a heat/mass transfer analogy. For example, in the case of a forced-convective (annular) flow around a cylindrical fuel specimen (in the laminar flow regime) (dropping the subscript i) [4],

$$k_m = \frac{4cD_{AB}}{d}, \tag{28}$$

where c is the molar concentration of gas around the fuel specimen ($= p_{tot}/RT$), D_{AB} is the binary diffusion coefficient of a FP (for the dominant chemical form) or UO_3 compound (A) in a carrier gas atmosphere (B), and d is the equivalent diameter. As discussed in Ref. [4], for a cladded fuel specimen, this coefficient represents an upper-bound value since it implicitly assumes that the mass transfer across the oxidized and cracked cladding offers little resistance. The mass transfer in the fuel-to-clad gap for the CEA fuel specimens, however, is less restricted (see Section 3.1.1) since the fuel specimens did not have any end caps. For the CRL test (see Section 3.1.2), the fuel specimen did not contain any cladding, and therefore Eq. (28) is directly applicable. The mass transfer coefficient for other flow conditions are given in Ref. [4].

From the Chapman–Enskog kinetic theory, the quantity cD_{AB} (in mol cm^{-1} s^{-1}) in Eq. (28) is given by [31]

$$cD_{AB} = 2.2646 \times 10^{-5} \frac{\sqrt{T(1/M_A + 1/M_B)}}{\sigma_{AB}^2 \Omega_{AB}}, \tag{29}$$

where T is in K, M is the molecular weight in g mol^{-1} and σ_{AB} is the collision diameter in Å. The collision integral Ω_{AB} is a function of the Lennard-Jones force constant ε_{AB}/κ [4],

$$\Omega_{AB} = \frac{1}{0.7049 + 0.2910 \ln(T\kappa/\varepsilon_{AB})}. \tag{30}$$

The combining laws for the parameters σ_{AB} and ε_{AB}/κ are based on the individual quantities

$$\sigma_{AB} = \tfrac{1}{2}(\sigma_A + \sigma_B), \tag{31}$$

$$\frac{\varepsilon_{AB}}{\kappa} = \sqrt{\frac{\varepsilon_A}{\kappa}\frac{\varepsilon_B}{\kappa}}, \tag{32}$$

which can be obtained from Ref. [21] where data exist. Unfortunately, these quantities are not known for many compounds. In this case, within the uncertainty of the present analysis, it can be assumed that $\Omega_{AB} \sim 1$. Alternatively, ε_A/κ can be obtained from a simple linear correlation with the molecular weight of the compound [21], from which Ω_{AB} follows via Eqs. (30) and (32). However, the linear correlation in Ref. [21] is only specifically valid for the noble gases and is not representative of all fission product species. This latter methodology typically yields a greater percent error difference (i.e., 19% ± one standard deviation of 12%) than the simple assumption of unity for the collision integral (i.e., 7% ± one standard deviation of 17%) when Ω_{AB} is evaluated from the existing data for ε_A/κ in Ref. [21]. Furthermore, the collision diameter σ_A (in Å) can be estimated from the liquid molar volume at the normal boiling point V_b (in cm^3 mol^{-1}) [31],

$$\sigma_A = 1.166 V_b^{1/3}. \tag{33}$$

For a given fission product or actinide compound, V_b can be obtained by a summation of the additive contributions

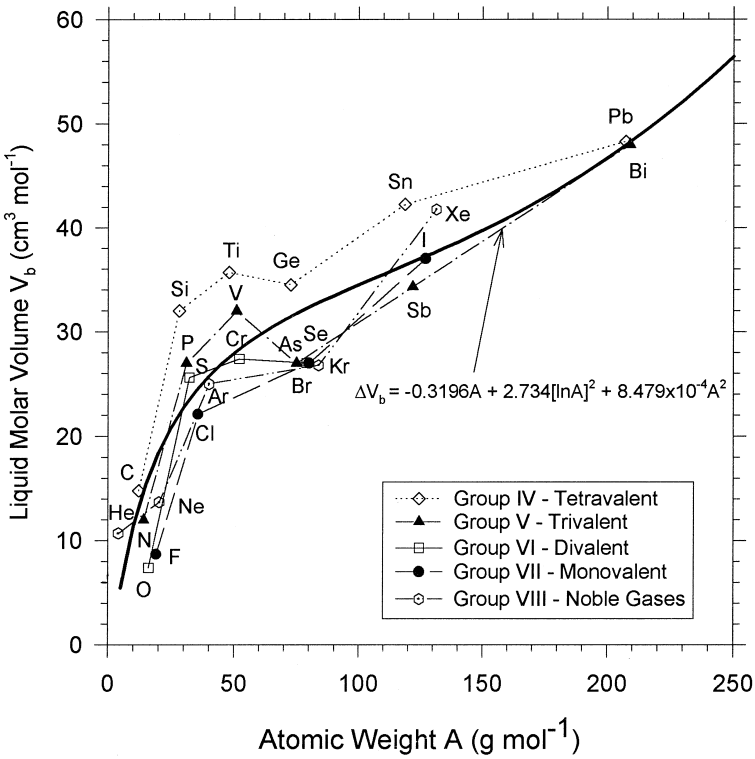

Fig. 1. Relation between Le Bas volumes and atomic weights.

of the individual atoms making up the compound [32–34]. For instance, a periodic relation exists where the atomic volume can be correlated with the atomic weight (and to a lesser extent with the periodic grouping, i.e., valence state) [32]. Hence, using the structural data of Le Bas as shown in Fig. 1 [32,33], an empirical correlation can be developed as a function of the atomic weight A (g mol^{-1}) for the prediction of the atomic volume contributions ΔV_b (cm^3 mol^{-1}),

$$\Delta V_b = -0.3196\,A + 2.734(\ln A)^2 + 8.479 \times 10^{-4} A^2. \quad (34)$$

In summary, using the available Le Bas structural data in Table 2, or Eq. (34) for any missing data, V_b can be determined additively for the fission product compound of interest (which exists as either a metal, oxide, hydroxide, etc.) or actinide compound (e.g., UO_3). In turn, σ_A can then be predicted from Eq. (33). This additive methodology yields an average error difference for σ_A of 17% as compared to the measured data in Ref. [21].

Table 2
Volume increments for the calculation of molar volumes

Element	Le Bas atomic volume increment, ΔV_b (cm^3 mol^{-1})
As	30.5
Br	27.0
I	37.0
Sb	34.2
Sn	42.3
H	3.7
O	7.4 (12.0 in acids)

2.3.2. Equilibrium partial pressure calculations

The FACT computer program EQUILIB was used to determine the thermodynamic equilibrium state of the FPs, including a calculation of the partial pressure of the gaseous compounds [11]. In the thermodynamic model, it is implicitly assumed that there is a closed system consisting of both fuel and FPs in a specific proportion, and a gaseous atmosphere of hydrogen/steam at a given system (hydrostatic) pressure and temperature. It is further assumed that all gaseous species behave as an ideal gas mixture. In addition, it is assumed that the liquid metallic elements, when this phase is present, behave as an ideal solution. For this single liquid phase, consisting of some 20 metallic elements (see Table 3), the activity of any one element would then be its mole fraction within the liquid. The presence of the ideal liquid solution, however, was not found in the majority of cases as it required very specific conditions of temperature and oxygen potential (i.e., a reducing atmosphere). All condensed species, composed of single metallic oxides, hydrides, or hydroxides; metallic

Table 3

Species considered in the FACT analysis

Gaseous species (173)

Am	AmO	AmO_2	Ba	$Ba(OH)_2$	Ba_2	Ba_2O	Ba_2O_2	BaH	BaI	BaI_2	$BaMoO_4$	BaO	BaOH	Ce
Ce_2	CeO	CeO_2H_2	CeO_3H_3	CeOH	CeTe	Cs	Cs_2	Cs_2I_2	Cs_2MoO_4	Cs_2O	Cs_2O_2	CsH	CsI	CsO
CsOH	$(CsOH)_2$	Eu	Eu_2O	Eu_2O_2	EuO	EuO_2H_2	EuO_3H_3	EuOH	EuTe	H	H_2	H_2O	H_2Te	H_2TeO_3
HI	HIO	HOO	HOOH	I	I_2	IO	La	La_2	La_2O	La_2O_2	LaO	LaO_2H_2	LaO_3H_3	LaOH
LaTe	Mo	Mo_2	Mo_2O_6	Mo_3O_9	Mo_4O_{12}	Mo_5O_{15}	MoI	MoI_2	MoI_3	MoI_4	MoO	MoO_2	MoO_2H_2	MoO_2I_2
MoO_3	MoOH	Nb	NbO	NbO_2	NbO_2H_2	NbOH	Nd	NdO	NdO_2	NdO_2H_2	NdO_3H_3	NdOH	NdTe	O
O_2	$O_2Mo(OH)_2$	O_3	O_4Sb_4	OH	Pr	PrO	PrO_2H_2	PrO_3H_3	PrOH	PrTe	Pu	PuO	PuO_2	PuO_3
$PuO_3(H_2O)$	Rh	RhO	RhO_2	RhO_2H_2	RhOH	Ru	RuO	RuO_2	RuO_2H_2	RuO_3	RuO_3OH	RuO_4	RuOH	Sb
Sb_2	Sb_4	SbH_3	SbI_3	SbO_2H_2	SbOH	SbTe	Sr	$Sr(OH)_2$	Sr_2	Sr_2O	SrH	SrI	SrI_2	SrO
SrOH	Te	Te_2	Te_2O_2	Te_2O_4	Te_5	TeI_4	TeO	TeO_2	TeO_2H_2	TeOH	$TeOI_2$	U	UO	UO_2
UO_2H_2	UO_3	$UO_3(H_2O)$	UOH	UTe	Y	Y_2	YO	YO_2H_2	YO_3H_3	YOH	YTe	Zr	ZrH	ZrI
ZrI_2	ZrI_3	ZrI_4	ZrO_2	ZrO	ZrO_2H_2	ZrOH	$ZrTe_2$							

Liquid species

Molten alloy components[a] (20)

Am	Ba	Ce	Cs	Eu	I_2	La	Mo	Nb	Nd	Pr	Pu	Rh	Ru	Sb
Sr	Te	U	Y	Zr										

Compounds (36)

$Ba(OH)_2$	BaI_2	BaO	Ce_2O_3	CeI_3	Cs_2MoO_4	Cs_2TeO_3	CsI	CsOH	Eu_2O_3	H_2O	HOOH	La_2O_3	LaI_3	MoO_3
Nb_2O_5	NbI_5	NbO	NbO_2	Nd_2O_3	NdI_3	Pr_2O_3	PrI_3	PuI_3	PuO_2	RuO_4	Sb_2O_3	Sb_2Te_3	SbI_3	$Sr(OH)_2$
SrI_2	SrO	TeO_2	UI_4	ZrI_2	ZrO_2									

Solid species (221)[b]

Am	Am(s2)	Am(s3)	Am_2O_3	AmO_2	$Ba(IO_3)_2(H_2O)$	$Ba(IO_3)_2$	$Ba(OH)_2(H_2O)_8$	$Ba(OH)_2$	Ba	BaH_2	BaI_2	$BaMoO_3$	$BaMoO_4$	BaO
(BaO)(UO_3)	(BaO)(ZrO_2)	BaO_2	BaTe	$Ce(IO_3)_3(H_2O)_2$	Ce	Ce(s2)	$Ce_{18}O_{31}$	Ce_2O_3	Ce_2Te_3	Ce_6O_{11}	CeH_2	CeI_3	CeO_2	CeTe
Cs	$Cs_2Mo_2O_7$	$Cs_2Mo_3O_{10}$	$Cs_2Mo_4O_{13}$	$Cs_2Mo_5O_{16}$	$Cs_2Mo_7O_{22}$	Cs_2MoO_4	Cs_2MoO_4(s2)	Cs_2O	Cs_2O_3	Cs_2Te	$Cs_2Te_2O_5$	$Cs_2Te_4O_{12}$	$Cs_2Te_4O_9$	Cs_2TeO_3
Cs_2TeO_4	$Cs_2U_{15}O_{46}$	$Cs_2U_2O_7$	$Cs_2U_4O_{12}$	$Cs_2U_4O_{12}$(s2)	$Cs_2U_4O_{13}$	$Cs_2U_5O_{16}$	$Cs_2U_6O_{18}$	$Cs_2U_7O_{22}$	$Cs_2U_9O_{27}$	Cs_2UO_4	$Cs_2Zr_2O_5$	$Cs_2Zr_3O_7$	Cs_2ZrO_3	Cs_3NbO_4
$Cs_4U_2O_7$	$Cs_4U_5O_{17}$	CsI	$CsNbO_3$	CsO_2	CsOH	CsOH(s2)	CsOH(s3)	$Eu(OH)_3$	Eu	Eu_2O_3	Eu_2O_3(s2)	Eu_3O_4	EuH_2	EuI_3
EuO	H_2O	H_2TeO_4	I_2	$La(IO_3)_3$	La	La(s2)	La(s3)	La_2O_3	La_2Te_3	LaH_2	LaI_3	LaTe	Mo	Mo_5Ru_3
MoI_2	MoI_3	MoI_4	MoO_2	MoO_3	$MoTe_2$	Nb	Nb_2O_5	NbI_5	NbO	NbO_2	NbO_2(s2)	NbO_2(s3)	Nd	Nd(s2)
Nd_2O_3	Nd_2O_3(s2)	$(Nd_2O_3)(ZrO_2)_2$	Np	NpO_2	$NpO_3(H_2O)$	Nd_2Te_3	NdH_2	NdI_3	NdI_3(s2)	NdTe	$Pr(OH)_3$	Pr	Pr(s2)	Pr_2O_3
Pr_2Te_3	Pr_6O_{11}	Pr_7O_{12}	PrH_2	PrI_3	PrO_2	PrTe	Pu	Pu(s2)	Pu(s3)	Pu(s4)	Pu(s5)	Pu(s6)	Pu_2O_3	Pu_5O_8
PuH_2	PuH_3	PuI_3	PuO_2	PuOI	Rh	Rh_2O	Rh_2O_3	RhO	RhO_2	RhTe	$RhTe_2$	Ru	RuO_2	RuO_4
$RuTe_2$	Sb	Sb_2O_3	Sb_2O_3(s2)	Sb_2O_4	Sb_2O_5	Sb_2Te_3	SbI_3	SbO_2	$Sr(IO_3)_2(H_2O)$	$Sr(IO_3)_2(H_2O)_6$	$Sr(IO_3)_2$	$Sr(OH)_2$	Sr	Sr(s2)
$SrCeO_3$	SrH_2	SrI_2	SrO	(SrO)(MoO_3)	(SrO)(ZrO_2)	SrO_2	SrTe	$SrUO_4$	Te	TeI_4	TeO_2	U	U(s2)	U(s3)
U_2Te_3	U_3O_8	U_3Te_4	U_3Te_5	U_3Te_7	U_4O_9	UH_3	UI_3	UI_4	UO_2	$UO_3(H_2O)$	$UO_3(H_2O)_2$	UO_3	URh_3	URu_3
UTe	UTe_2	UTe_3	$Y(IO_3)_3$	$Y(OH)_3$	Y	Y(s2)	Y_2O_3	Y_2O_3(s2)	$(Y_2O_3)(ZrO_2)_2$	Y_2Te_3	YH_2	YH_3	YI_3	YTe
Zr	Zr(s2)	ZrH_2	ZrI_2	ZrI_3	ZrI_4	ZrO_2	ZrO_2(s2)	ZrO_2(s3)	$ZrTe_2$	$ZrTe_3$				

[a]These species were treated as members of the ideal solution (see text).

[b](s2) and (s3) correspond to solids with different crystalline structures.

CALPHAD Vol. 21, No. 4, pp. 513–528, 1997

Table 4
Moles of actinides and fission product elements used in the FACT analysis

Element	CANDU channel	PWR core
Actinides		
Uranium[a]	1015	279673
Neptunium	0.096	184
Plutonium	2.754	3423
Americium	0.0064	51
Fission products		
Cerium	0.824	1431
Yttrium	0.215	378
Tellurium	0.138	269
Lanthanum	0.332	638
Zirconium	1.442	2823
Barium	0.389	798
Ruthenium	0.899	1878
Molybdenum	1.150	2480
Praseodymium	0.265	565
Strontium	0.421	728
Iodine	0.077	135
Neodymium	0.859	1845
Niobium	0.043	32
Cesium	0.745	1591
Rhodium	0.166	287
Antimony	0.006	10
Europium	0.025	95

[a]Assumed chemical form for FACT analysis is UO_2.

compounds; or spinels, are further considered to be mutually insoluble stoichiometric compounds. The Gibbs phase rule limits the maximum number of phases possible in the calculation. Similar assumptions were also considered in the earlier analysis of Cubicciotti et al. [5–7]. In view of the large number of components and species (see Table 3), and the incompleteness of data on non-ideal behavior (i.e., for the heavy metal compounds), these assumptions were considered appropriate to identify major fission product species, and to provide a good basis for further study and model refinement. Moreover, non-ideal behavior is in many circumstances a second-order effect. Experimental work is currently underway to study the non-ideal, multi-component solution phase, i.e., FACT has the computational capability to incorporate non-ideal modelling once thermodynamic data become available. Thus, the present analysis provides for the best estimation of fission product partial pressures that are currently possible.

For the CANDU reactor analysis, the FP inventory is assumed to be present in a single fuel channel (13 bundles), as calculated with the ORIGEN code for a Bruce A reactor (with an equilibrium burnup of 100 MWh/kg U) (see Table 4). The FP inventory, assumed to be present in an entire PWR core, was calculated with the MARISE computer code for a commercial French 900 MWe pressurized water reactor (PWR) with a fuel core of 70,000 kg of uranium and burnup of 35 MWd/kg U (see Table 4) [35]. Within the limitations of the FACT architecture, 23 elements were considered for a given calculation which included: the actinides (U, Np, Pu, Am), FPs (Ce, Y, Te, La, Zr, Ba, Ru, Mo, Pr, Sr, I, Nd, Nb, Cs, Rh, Sb, Eu), and atmospheric constituents (H_2, H_2O). The chemical effects of the graphite coating used in CANDU fuel as a lubrication interlayer between the fuel and cladding, has not been considered in the present analysis since this material is rapidly washed out or chemically decomposes when the rod defects during normal or accident situations. For instance, during the initial phase of high-temperature transients after the fuel rod defects, steam will react with the graphite coating to form gaseous CO/CO_2 which will quickly dissipate from the rod.

In order to cover various accident scenarios, the calculations were performed over a wide range of input parameters. As shown in Table 5, the matrix parameters included: (i) temperatures from 1000 to 3000 K; (ii) total system pressure of 1 atm (typical of annealing tests) for PWR fuel and 1, 10 and 30 atm for CANDU fuel; (iii) hydrogen-to-steam ratios (i.e., H_2/H_2O) of 100 000, 10 000, 1000, 100, 10, 1, 0.1 and 0.01; and (iv) FP-to-gas atmosphere ratios (i.e., $Cs/(H_2 + H_2O)$) of 10^{-6}, 10^{-5} and 10^{-4}. The $Cs/(H_2 + H_2O)$ ratios are representative of conditions that develop as the original coolant vaporizes during blowdown in the PWR vessel or CANDU fuel channel, as well as those conditions which arise in the annealing tests. Similar ratios were also considered by Cubicciotti et al. [7]. This matrix yields a total of 744 cases for PWR fuel and 2232 cases for CANDU fuel.

The present treatment includes a total of 450 different compounds, with the corresponding distribution of 23 elements over 173 gaseous species and 277 possible condensed (liquid and solid) species (see Table 3). The partial pressures of the various FP compounds calculated for each set of conditions of H_2/H_2O ratio and $Cs/(H_2 + H_2O)$ ratio in Table 5 can be summed for each of the four actinide and 17 FP elements. Several calculations are

Table 5
Matrix of conditions for FACT calculations[a]

Fuel type	Temperature (K)	$Cs/(H_2 + H_2O)$ molar ratio	H_2/H_2O molar ratio
CANDU, PWR	1000–2000 (steps of 50 K), 2000–3000 (steps of 100 K)	10^{-4}, 10^{-5}, 10^{-6}	10^5, 10^4, 10^3, 10^2, 10, 1, 10^{-1}, 10^{-2}

[a]System pressure of 1 atm for PWR fuel and 1, 10 and 30 atm for CANDU fuel.

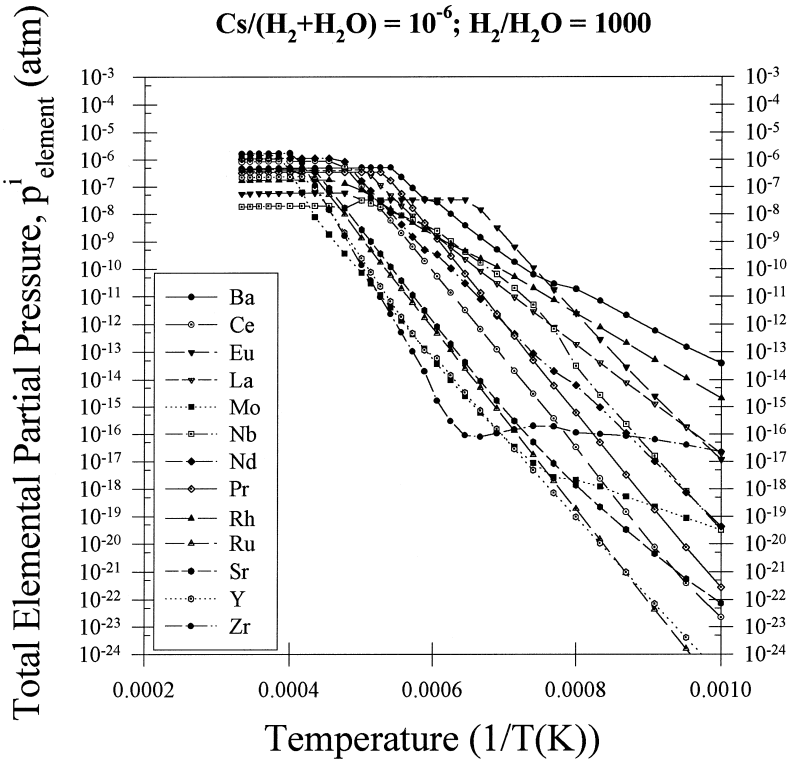

Fig. 2. Total elemental partial pressure (calculated by FACT) versus temperature for low-volatile fission products at a total system pressure of 1 atm for CANDU fuel.

shown as a function of temperature for various H_2/H_2O and $Cs/(H_2 + H_2O)$ ratios for CANDU (Fig. 2) and PWR (Fig. 3) fuel. As discussed in Ref. [5], for different fuel burnups, the results can be scaled accordingly. However, no consideration has been given in the present analysis to account for the changing fission product distribution as fission products are lost from the system as a result of vapor transport.

2.3.3. Analytical representation: Method of chemical potentials (MOCP)

The partial pressure of an individual compound can also be analytically extracted from the FACT analysis in terms of a stand-alone algorithm [36]. For example, for the general reaction for formation of a compound from the elements,

$$xA + yB + zC \overset{K}{\Leftrightarrow} A_xB_yC_z, \tag{35}$$

it follows that

$$K = \frac{p_{A_xB_yC_z}}{(p_A)^x (p_B)^y (p_C)^z} = \exp\left(-\frac{\Delta G^0}{RT}\right). \tag{36}$$

Here R is the ideal gas constant, T is the temperature, K is the equilibrium constant for Eq. (35) and ΔG^0 is the standard Gibbs energy change of the reaction which can be computed from the standard ('absolute') Gibbs energy equations for the elements and compounds,

$$\Delta G^0 = G^0_{A_xB_yC_z} - xG^0_A - yG^0_B - zG^0_C. \tag{37}$$

These ('absolute') Gibbs energy equations represent the combination of enthalpy change (ΔH^0) and absolute entropy (S^0) by the relation

$$G^0 = \Delta H^0 - TS^0 = A + BT + CT^2 + \frac{D}{T} + ET\ln T + FT^3 + GT^{1/2} + \frac{H}{T^2} + I\ln T + JT^4. \tag{38}$$

The apparent mixing of enthalpy change and absolute entropy combines in Eq. (38) to yield the correct ΔG^0 for the process in Eq. (35). The use of Eq. (38) is simply a convenience in computing ΔG^0. The coefficients for the Gibbs energy data (for G^0 given in J mol^{-1}) in the second relation of Eq. (38) are taken from the FACT database in order to calculate the partial pressures of the gaseous

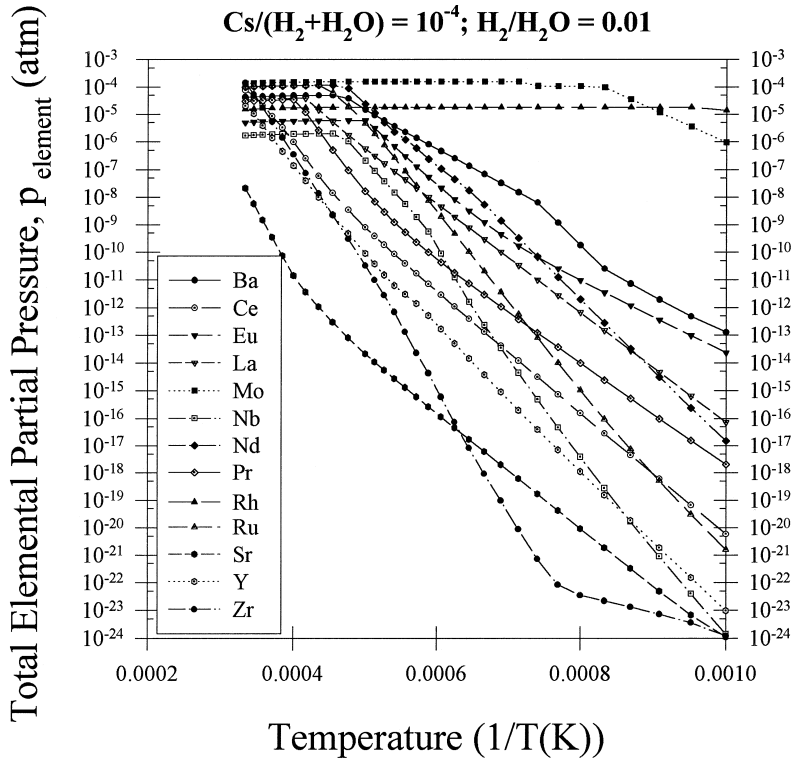

Fig. 3. Total elemental partial pressure (calculated by FACT) versus temperature for low-volatile fission products at a total system pressure of 1 atm for PWR fuel.

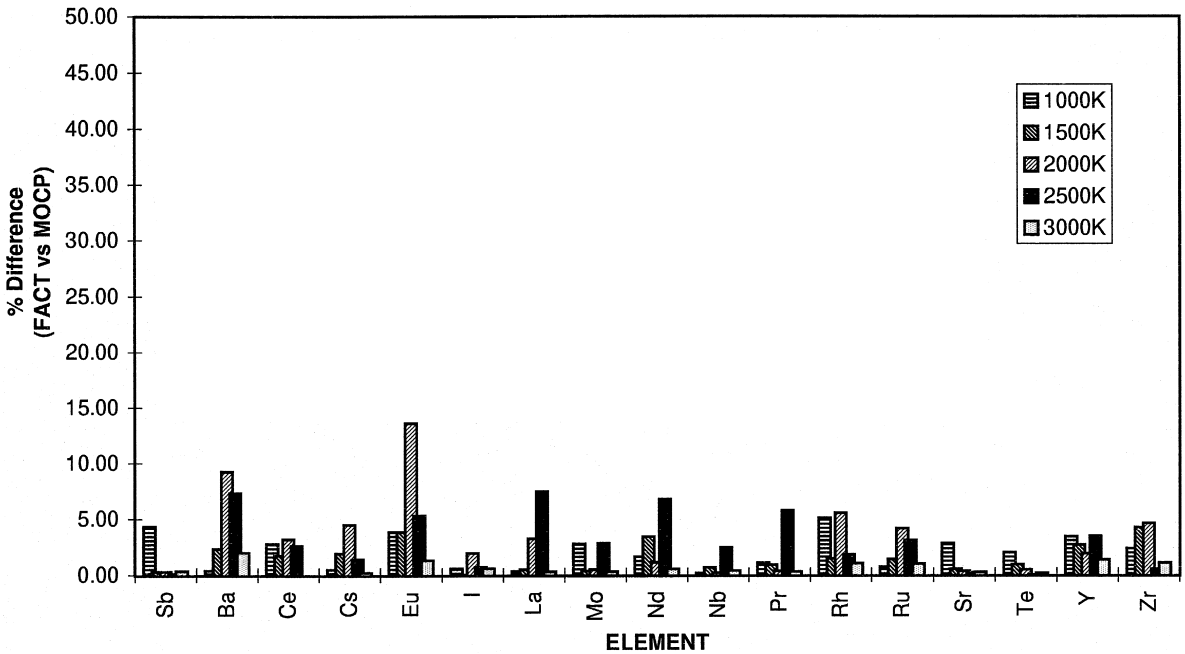

Fig. 4. Typical percent-error difference between FACT and MOCP for total elemental partial pressure calculations. This case is for CANDU fuel, with $H_2/H_2O = 1$ and $Cs/(H_2 + H_2O) = 10^{-4}$.

compounds in Table 3. Eq. (36) can therefore be equivalently written as

$$\log p_{A_xB_yC_z} = x \log p_A + y \log p_B + z \log p_C - \frac{\Delta G^0}{2.303RT}. \quad (39)$$

The partial pressures of individual elemental species i at equilibrium, p_i (for $i = A, B, C, \ldots$) can be represented from the FACT results using a Legendre–Fourier series representation for a given H_2/H_2O and $Cs/(H_2 + H_2O)$ situation,

$$\log(p_i) = \sum_{m=0}^{11} a_m P_m(T_r), \quad (40)$$

where P_m is a Legendre polynomial of order m and $T_r = T/3000$. A reduced temperature (T_r) is required so that Eq. (40) is an orthogonal series over the given temperature range. To provide an accurate evaluation of Eq. (40), without the need to carry a large number of significant figures, the Legendre polynomials can be evaluated from the specific values of the two lower-order ones at a given temperature using the recursive relation [37]

$$P_0 = 1, \qquad P_1 = T_r \quad \text{and}$$

$$P_{m+1}(T_r) = \frac{(2m+1)T_r P_m(T_r) - mP_{m-1}(T_r)}{m+1} \times (m = 1, 2, \ldots, 10). \quad (41)$$

The coefficients (a_m) in Eq. (40) covering the full range of conditions in Table 5, plus those for the Gibbs energy data in Eq. (38), total about 23 000 and are tabulated in Ref. [38] and stored in an electronic database form (Microsoft Access program) for efficient use in a computer code. Thus, using Eq. (40) for the fitted partial pressure functions of the individual elements, with the Gibbs energy data for Eq. (37), the partial pressures of all the individual compounds can be explicitly recalculated from Eq. (39) [38]. On summing the partial pressures for a compound containing a common element i, one also obtains an evaluation of the total elemental partial pressure as depicted in Figs. 2 and 3,

$$p^i_{\text{element}} = \sum_{j = \text{compound containing element } i} p_j. \quad (42)$$

As shown in Fig. 4 for a representative case, the average percent difference between FACT and the total pressure reconstitution of Eq. (42) is typically $\sim 3\%$ over the full range of temperature for the 17 FP elements. The inability to refit the data more precisely is due to the change in condensed phase assemblage as temperature alters, which causes small kinks in an otherwise monotonic function (see Fig. 5). Thus, Eqs. (39) and (42) provide a closed-form algorithm to rapidly re-construct the total pressure of an element and all partial pressures of the various compounds containing the element, including the dominant chemical form (i.e., the maximum p_j for a given element i) for a particular reactor accident condition of temperature, H_2/H_2O ratio and $Cs/(H_2 + H_2O)$ ratio. The purpose of this procedure is to provide a simple algorithm for compaction of the extensive FACT results with the ability for interpolation over the full range of temperature without the necessity of the time-consuming, Gibbs-energy minimization [38]. The proposed function in Eq. (40) is well-behaved, as shown for example in Fig. 5, and therefore the given algorithm also yields an accurate interpolation between the stated temperatures as compared to actual FACT

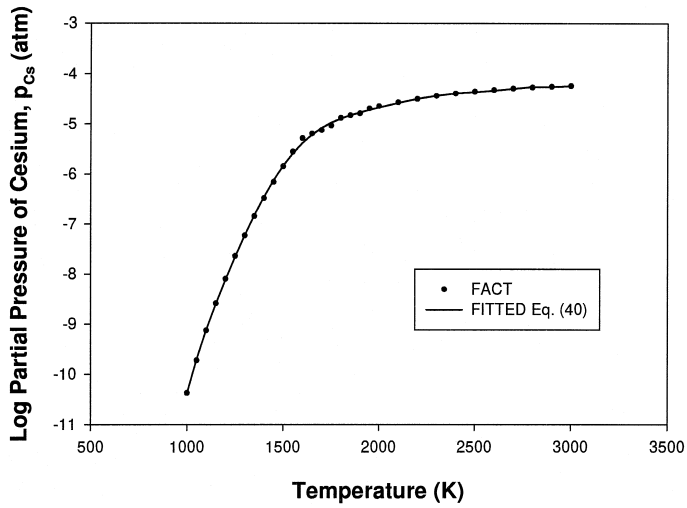

Fig. 5. Example of the fitting of Eq. (40) for the Cs partial pressure to actual FACT calculations as a function of temperature for CANDU fuel, with $H_2/H_2O = 1$ and $Cs/(H_2 + H_2O) = 10^{-4}$.

calculations (see Table 6). This means that the full consideration of the basic premise of low-volatile FP release, based on the assumption of local equilibrium at the point of origin, can be fully explored where the source partial pressure and dominant chemical form of the fission products are quickly retrievable in a more complex model which deals with mass transfer from the source to the environment (see Section 2.3).

3. Comparison of model to experiment

The low-volatile, fission-product release and fuel volatilization model can be applied to annealing experiments conducted at the Commissariat à l'Energie Atomique (CEA) and the Chalk River Laboratories (CRL). Experiments conducted at the Oak Ridge National Laboratory (ORNL) [1,22] have not been considered in the present analysis because of significant steam bypass in the test facility, and the complicating effect of fuel-to-clad gap transport, i.e., the ORNL fuel specimens contained end caps in contrast to those used at the CEA (Section 3.1.1) [2]. Also no kinetic data were available in the ORNL experiments for the low-volatile fission products (only end-of-test release measurements were made for ^{125}Sb, ^{154}Eu and ^{106}Ru) due in part to the fact that the fuel was not re-irradiated before the experiment.

A brief description of the various CEA and CRL test conditions are given in Section 3.1. The model is compared with the experimental results in Section 3.2.

3.1. Experiment description

Several high-temperature annealing tests were conducted at atmospheric pressure at the CEA using short-length, Zircaloy-clad, fuel specimens in both a hydrogen (Heva-6) and steam atmosphere (Vercors-2), and at the CRL using a small fuel fragment in a steam environment (MCE2-T19). The details of the fuel specimen, pretest irradiation conditions and experimental parameters are briefly summarized in Table 7.

3.1.1. CEA tests

A complete description of the experiments are given in Refs. [2,4,22]. The fuel specimens were cut from spent commercial rods, and consisted of three pellets contained in the original Zircaloy cladding. A half-pellet of depleted UO_2 was placed at each end of the fuel stack, which was held in place by crimping the ends of the cladding (i.e., no end caps were used). The total fissile height was about 45 mm and the total sample height was $\sim$80 mm. In order to restore the short-lived inventory after the long cooldown periods, the fuel samples were re-irradiated in the SILOE experimental reactor for $\sim$6 days at 8 W/cm for the Heva test and at 15 W/cm for the Vercors test.

In the Heva-6 experiment (see Table 7 and Fig. 6), an initial phase was performed to oxidize the zircaloy cladding during which the fuel specimen experienced a mixture of steam (25 mg/s) and hydrogen (0.2 mg/s) at a temperature of $\sim$1570 K for 60 min. The sample was then exposed to a reducing atmosphere of helium (8 mg/s) and hydrogen (0.2 mg/s) and ramped in temperature (1.4 K/s), where it was maintained at a high-temperature level of 2320 K for $\sim$30 min. During this second phase, it is believed that the carrier gas (helium and H_2) had an impurity level of $\sim$50 ppm of water vapor [2].

The Vercors-2 experiment (see Table 7 and Fig. 6) was carried out at a low-temperature plateau of $\sim$1780 K for 30 min in a gas flow mixture of steam (25 mg/s), hydrogen (0.05 mg/s) and helium (0.5 mg/s). The fuel was then ramped in temperature (1.6 K/s), and experienced a high-temperature level of $\sim$2100 K in a predominantly oxidizing atmosphere of steam (25 mg/s) and hydrogen (0.5 mg/s) for 13 min.

3.1.2. CRL test

In the MCE2-T19 experiment, the fuel specimen was obtained by cutting a section of a spent element of a Bruce-type design. The fuel fragment was roughly cylindrical in shape ($\sim$2.2 mm diameter and 5 mm length), with a weight of 0.200 g and a burnup of 457 MW h/kg U. The sample was introduced into a flowing mixture of argon/2% H_2 (40 ml/min at STP) and ramped in temperature at a rate of $\sim$0.15 K/s to 2300 K (see Table 7 and Fig. 6). After the temperature plateau had been reached, the fuel was exposed to an oxidizing mixture of steam (15 g/h) and argon (40 ml/min at STP) for 7 min. The atmosphere was then replaced by an argon/2% H_2 flow (40 ml/min at STP) and the temperature decreased at the same ramp rate as during the heating period. The oxygen partial pressure of the atmospheric composition was continuously monitored with yttria-stabilized zirconia oxygen sensors at upstream and downstream locations from the fuel specimen (see Fig. 6) [26]. Fission products released from the fuel specimen were swept away such that a gamma-ray spectrometer, collimated at the sample location, provided information on the kinetic release behavior.

Table 6
Comparison of the method of chemical potentials (MOCP) (interpolated) with FACT calculations[a]

Temperature (K)	Vapor pressure of $BaMoO_4$ (atm)		Δ%
	FACT	MOCP	
1225	2.86×10^{-13}	2.60×10^{-13}	9.2
1725	4.17×10^{-8}	4.39×10^{-8}	−5.1
2250	3.25×10^{-6}	3.61×10^{-6}	−11.0
2750	3.84×10^{-7}	4.27×10^{-7}	−11.3

[a]For CANDU fuel case with $H_2/H_2O = 1$ and $Cs/(H_2 + H_2O) = 10^{-4}$.

Table 7
Summary of experimental parameters for CEA and CRL tests

Parameter	CEA tests[a]		CRL test
	Heva-6	Vercors-2	MEC2-T19
Test description	fission product release at 2370 K in H_2 with irradiated/rerradiated zircaloy-clad fuel specimen	fission product release at 2150 K in H_2O and H_2 with irradiated/reirradiated zircaloy-clad fuel specimen	fission product release at 2300 K in H_2O with irradiated fuel-fragment specimen
Fuel specimen			
fuel type	Fessenheim 1/2	Bugey/3	NRU XM
rod identification	C12 (FDC 57)	C19 (FGC 53)	AC-19
enrichment (wt% ^{235}U)	3.1	3.1	1.38
clad outer diameter (mm)	9.50	9.50	–
pellet/fragment diameter (mm)	8.19	8.19	~ 2.2
pellet/fragment length (mm)	13.96	13.96	~ 5
fissile length (mm)	46	44	–
sample height (mm)	80	80	–
Specimen weight (g)			
pretest	–	–	0.200
posttest	–	–	0.046
Geometrical surface-to-volume ratio (m^{-1})[b]	532	534	1890
Surface area (m^2)	1.18×10^{-3}	1.13×10^{-3}	3.46×10^{-5}
Irradiation data			
burnup (MWd/kg U)	36.7	38.3	19.0
average heat rating/discharge linear power (kW/m)	18.5/–	–/–	–/32.1
cooling period (y)	7	7	–
grain radius (μm)[c]	7.5	7.5	11.8
Test conditions[d]			
channel diameter (mm)[e]	25	25	4.75
test date	3/88	6/90	5/92
temperature rise (K/s)	1.4	1.6	0.15
maximum temperature (K)	2370	2150	2300
time at high-temperature plateau (s)	1800	780	420
flow rate (mg/s)			
H_2	0.2	0.5	0
H_2O	0	25	4.17

[a] Taken from Refs. [2,4,22].
[b] For the fuel oxidation model, S/V is taken as 3 times $(S/V)_{\text{geometrical}}$.
[c] Mean grain radius = (measured grain size × 1.570)/2 (see Ref. [39]).
[d] For CRL test: temperature ramp in argon-2% H_2 (40 ml/min at STP) and temperature plateau for 7 min in steam (15 g/h) and argon (40 ml/min at STP).
[e] For the calculation of the mass transfer coefficient, the equivalent diameter (d) is equal to the channel diameter minus the fuel (rod) diameter.

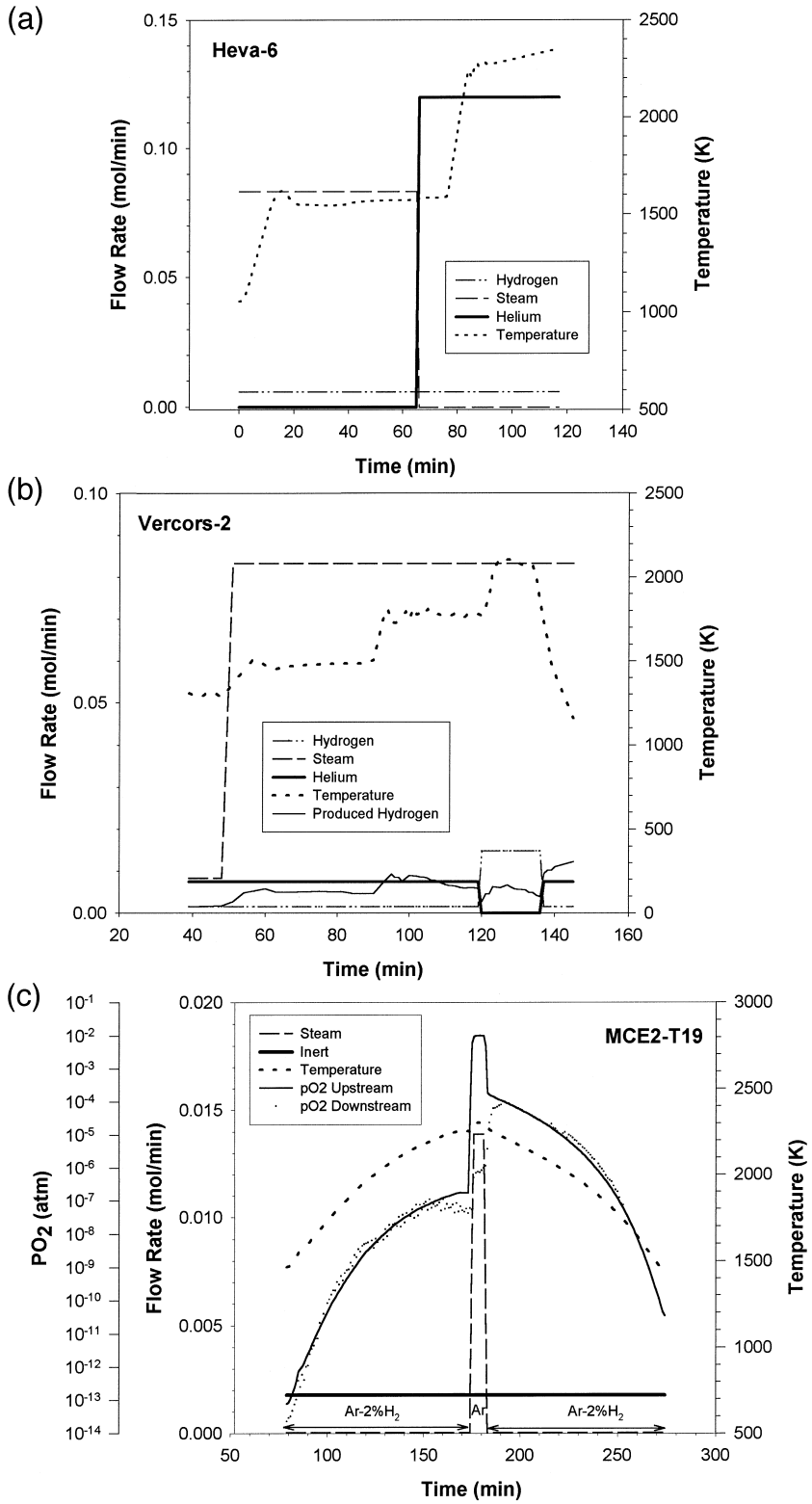

Fig. 6. Input atmospheric flow rate, hydrogen production rate, upstream and downstream oxygen partial pressure and temperature histories for (a) Heva-6, (b) Vercors-2 and (c) MCE2-T19 tests.

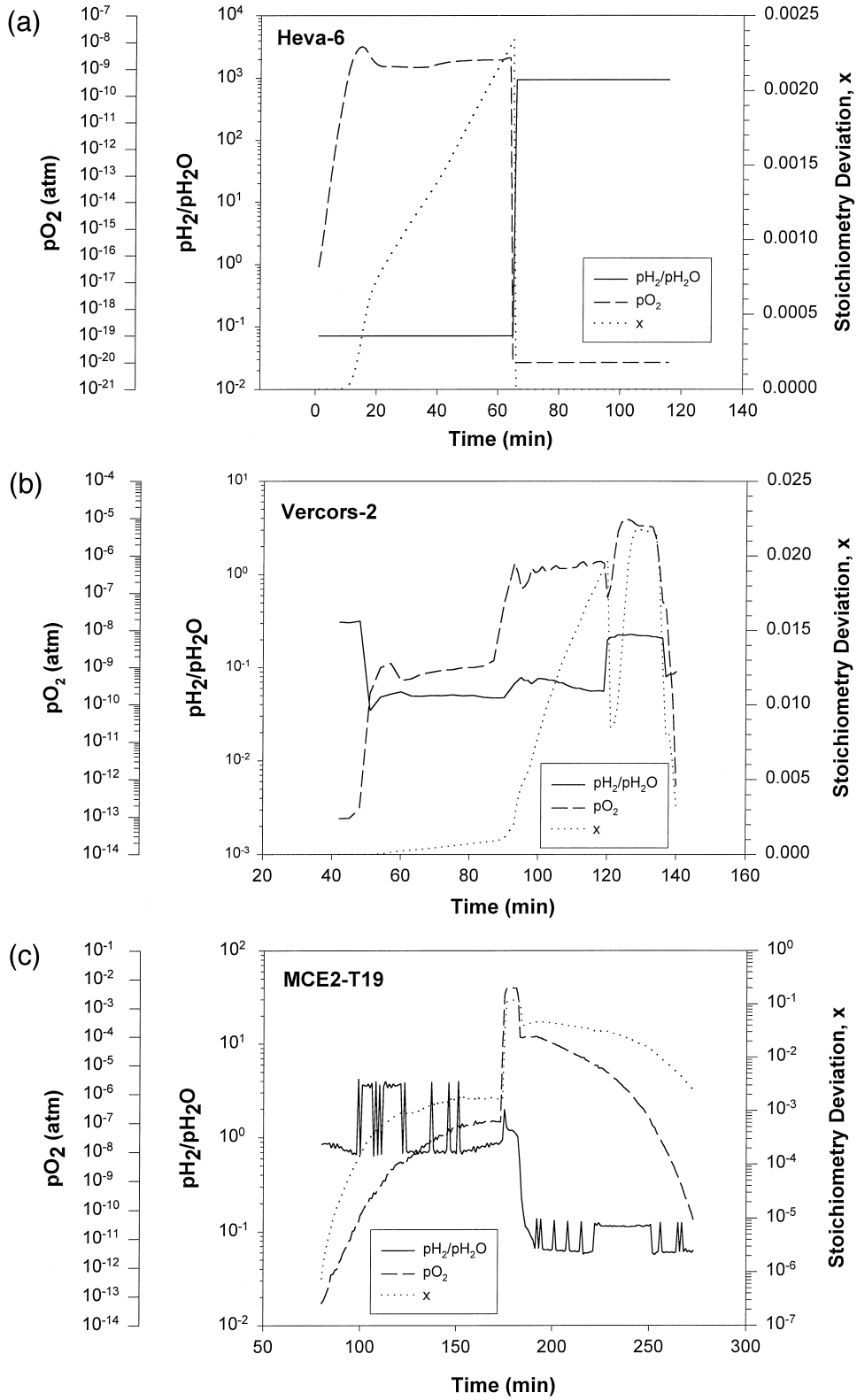

Fig. 7. Oxygen partial pressure, H_2/H_2O partial pressure ratio and stoichiometry deviation histories for (a) Heva-6, (b) Vercors-2 and (c) MCE2-T19 tests.

3.2. Model application

For the given atmospheric and temperature conditions in Fig. 6, the model of Eqs. (5), (6), (9), (11) and (12) yields the oxygen partial pressure, hydrogen-to-steam partial pressure ratio and stoichiometry deviation kinetics as shown in Fig. 7 for the three experiments [38]. These calculations are based on the methodology in Ref. [2] to account for hydrogen production from the clad/steam reaction for the CEA tests. The effect of steam bypass in the CEA experimental facility has also been considered in the present analysis based on the original analysis in Ref. [2] (see also Ref. [38]). For the CRL test, the measured p_{O_2} data were directly employed. Using the fission-product diffusion model (Section 2.1), the fuel volatilization/matrix stripping model (Section 2.2), the fission-product vaporization model (Section 2.3), and the fission product inventories (N_{go}) of Table 8, the predicted release fractions were calculated for the various release processes (see Table 9) [38]. For the noble gas (i.e., xenon) prediction, only the diffusion model was utilized. In the present analysis, the data in Table 7 were employed for the geometrical surface area (S), the effective surface-to-volume ratio (S/V), the grain radius (a) and the equivalent diameter (d). The binary diffusion coefficient was evaluated for the case of a trace fission-product species diffusing in the carrier gas mixture of Fig. 6 according to the combining law [4]

$$\frac{1-x_A}{D_{AB}} = \sum_{\substack{j=1 \\ j\neq A}}^{n} \frac{x_j}{D_{Aj}}, \tag{43}$$

where j refers to the components of the gas mixture, and x_j and x_A are the mole fractions of the gas components and fission products, respectively. Eq. (43) results from the Stefan–Maxwell equations for multi-component diffusion in which the various gas constituents move with the same velocity [31].

The equilibrium partial pressures ($p^i_{element}$) were derived as described in Section 2.3.3 for the hydrogen-to-steam partial pressure ratio in Fig. 7 and a fixed $Cs/(H_2 + H_2O + inert)$ molar ratio. In the case of an excessive partial pressure of inert gas (e.g., He), the equilibrium calculations as detailed previously may be affected to a modest degree although the validation does not reveal this. The $Cs/(H_2 + H_2O + inert)$ ratio was determined by dividing the 'exposed' molar inventory of cesium by the integrated gas flow rate, where the integration starts at a time when the volatile release is first observed to occur. The 'exposed' cesium inventory is estimated as the total quantity (N_{go}) in Table 8 times the diffusive release fraction (F_d) in Table 9. This latter calculation accounts for the fact that not all of the fission product inventory is in contact with the gas atmosphere, where it is implicitly assumed that all fission product species have roughly the same diffusion coefficient in the fuel matrix. This assumption is supported by observed kinetic data, where a similar release behavior was observed for ^{131}I, ^{137}Cs and ^{140}Ba in the Heva-6 test, and for ^{132}Te, ^{133}I, ^{135}Xe and ^{137}Cs in the Vercors-3 test, after the Zircaloy cladding had been oxidized [4]. The molar ratio $Cs/(H_2 + H_2O + inert)$ is therefore taken as 3.3×10^{-5}, 3.0×10^{-5} and 4.9×10^{-6}, respectively, for the Heva-6, Vercors-2 and MCE2-T19 tests. Model parameters, representative of the high-temperature plateau region in Fig. 6 for each experiment, are shown in including: the dominant chemical form of the fission-product compound (calculated by MOCP), the liquid molar volume of the fission-product compound (V_b),

Table 8
Initial fission product inventory in annealing tests

Element	Inventory, N_{go} (atom)		
	CEA tests		CRL test
	Heva-6	Vercors-2	MCE2-T19
Antimony	3.74×10^{18}	1.24×10^{18}	–
Barium	1.41×10^{20}	1.37×10^{20}	–
Cerium[a]	2.85×10^{20}	2.74×10^{20}	8.17×10^{17}
Cesium	2.67×10^{20}	2.51×10^{20}	8.71×10^{17}
Europium[a]	1.6×10^{19}	1.5×10^{19}	4.52×10^{16}
Iodine	2.76×10^{19}	2.63×10^{19}	–
Molybdenum	5.14×10^{20}	4.99×10^{20}	–
Niobium	–	–	1.61×10^{16}
Praseodymium	–	–	3.28×10^{17}
Rhodium	–	–	2.39×10^{17}
Ruthenium	4.54×10^{20}	3.14×10^{20}	1.14×10^{18}
Tellurium	5.57×10^{19}	5.38×10^{19}	–
Zirconium	–	–	1.56×10^{18}

[a] Estimated using the relative ratio of cesium to the given isotope of interest in Table 4.

Table 9
Comparison between measured and predicted release fractions

Chemical species (isotope)	Fractional release (%)																	
	Heva-6						Vercors-2						MCE2-T19					
	predicted[a]					measured[b]	predicted[a]					measured[b]	predicted[a]					measured
	RLS	F_d	F_{vol}	F_v	F	F	RLS	F_d	F_{vol}	F_v	F	F	RLS	F_d	F_{vol}	F_v	F	F
Xe(135)	D	35	–	–	35	15	D	30	–	–	30	23	–	–	–	–	–	–
Sb(125)	ZT	35	2.6×10^{-5}	24	0	0	ZT	30	0.05	34	6.2	7	–	–	–	–	–	–
Ba(140)	V	35	2.6×10^{-5}	32	32	27	V	30	0.05	6.9	6.9	~ 4	–	–	–	–	–	–
Ce(144)	V	35	2.6×10^{-5}	7.6	7.6	0	V	30	0.05	0.0013	0.0013	~ 0	V	96	70	4.6	5	~ 25[c]
Cs(137)	D	35	2.6×10^{-5}	48	35	30	V	30	0.05	18	13	30	D/MS	96	70	100	99	98
Eu(154)	V	35	2.6×10^{-5}	26	25	5	V	30	0.05	5.9	5.9	~ 0	D/MS	96	70	100	99	0
I(131)	D	35	2.6×10^{-5}	46	35	30	V	30	0.05	19	17	23	–	–	–	–	–	–
Mo(99)	V	35	2.6×10^{-5}	12	1.2	4	V	30	0.05	18	16	15	–	–	–	–	–	–
Nb(95)	–	–	–	–	–	–	–	–	–	–	–	–	D/MS	96	70	100	99	46
Ru(106)	V	35	2.6×10^{-5}	0.2	0.2	0	V	30	0.05	0.067	0.067	~ 0	V	96	70	39	39	81[c]
Te(132)	ZT	35	2.6×10^{-5}	62	22	11	ZT	30	0.05	25	9.8	18	–	–	–	–	–	–
Zr(95)	–	–	–	–	–	–	–	–	–	–	–	–	V	96	70	0.08	0.08	0

[a]RLS = rate-limiting step (ZT = zircaloy trapping, V = vaporization, D = diffusion, MS = matrix stripping). F_d = diffusion release fraction (all species are assumed to have the same diffusion coefficient as cesium). F_{vol} = fuel volatilization release fraction (the matrix stripping release fraction is assumed to be the same as the volatilization release fraction). F_v = fission-product vaporization release fraction. F = overall release fraction.
[b]Taken from Ref. [22].
[c]Inferred from the release behavior of the daughter isotopes ^{144}Pr and ^{106}Rh (see text and Appendix A).

Table 10
Calculation of vaporization model parameters for annealing tests[a]

Fission product																				
dominant compound			liquid molar volume, V_b ($cm^3\ mol^{-1}$)			collision diameter, σ_A (Å)			Lennard-Jones force constant, ε_A/κ (K)			binary diffusivity, cD_{AB} ($\times10^{-3}$ mol m^{-1} s^{-1})			mass transfer coefficient, $k_l m$ (mol m^{-2} s^{-1})			Total element vapor pressure, $p^i_{element}$ (atm)		
H-6	V-2	T19	H-6	V-2	T19	H-6	V-2	T19	H-6	V-2	T19	H-6	V-2	T19	H-6	V-2	T19	H-6	V-2	T19
Sb	Sb	–	34.2	34.2	–	3.06	3.06	–	2195	2195	–	10.4	3.44	–	2.70	0.89	–	2.04×10^{-7}	1.91×10^{-7}	–
Ba	$Ba(OH)_2$	–	38.3	60.5	–	4.15	4.11	–	2080	1148	–	7.37	2.54	–	1.90	0.66	–	1.54×10^{-5}	1.54×10^{-5}	–
CeO	CeO	CeO	46.1	46.1	46.1	4.18	4.18	4.18	[b]	[b]	[b]	4.86	2.51	2.66	1.26	0.65	4.17	1.25×10^{-5}	1.26×10^{-8}	3.03×10^{-7}
Cs	CsOH	CsOH	38.1	49.2	49.2	5.06	4.08	4.08	1188	1046	1046	6.03	2.52	2.96	1.56	0.65	4.64	3.15×10^{-5}	2.90×10^{-5}	4.70×10^{-6}
Eu	$Eu(OH)_2$	EuOH	40.0	62.2	51.1	3.99	4.62	4.33	[b]	[b]	[b]	5.15	2.19	2.33	1.33	0.57	3.66	1.87×10^{-6}	1.87×10^{-6}	1.84×10^{-7}
I	I	–	37	37	–	4.61	4.61	–	316	316	–	7.64	2.79	–	1.97	0.72	–	2.65×10^{-6}	2.47×10^{-6}	–
Mo	MoO_3H_2O	–	34.1	71.1	–	2.46	4.35	–	5656	660	–	11.9	2.67	–	3.08	0.69	–	6.18×10^{-9}	4.32×10^{-5}	–
–	–	NbO_2	–	–	48.6	–	–	4.25	–	–	[b]	–	–	2.64	–	–	4.14	–	–	1.94×10^{-7}
Ru	RuOH	RuOH	34.6	45.7	45.7	2.34	4.17	4.17	5050	[b]	[b]	12.6	2.55	2.71	3.26	0.66	4.26	1.84×10^{-7}	8.33×10^{-7}	3.86×10^{-6}
Te	Te	–	37.3	37.3	–	3.35	3.35	–	1387	1387	–	9.87	3.34	–	2.55	0.86	–	5.72×10^{-6}	5.08×10^{-6}	–
–	–	ZrO_2	–	–	48.4	–	–	3.21	–	–	10146	–	–	2.90	–	–	4.55	–	–	1.51×10^{-8}

[a]The parameters correspond to the high-temperature plateau in Heva-6 (H-6) at 2300 K, Vercors-2 (V-2) at 2100 K and MCE-T19 (T19) at 2300 K.
[b]Not available (no measured data). Since this parameter is needed for the calculation of Ω, it is therefore assumed that Ω is approximately unity.

the collision diameter (σ_A) and Lennard-Jones force constant (ε_A/κ) of the fission-product compound, the binary diffusion coefficient parameter (cD_{AB}), the mass transfer coefficient (k_m) and the total partial pressure of all fission products containing a given element ($p^i_{element}$).

3.3. Discussion

As shown in Table 9, the overall release fractions (F) that are predicted for most of the observed fission products are in good agreement (typically within a factor of two) with the measured results over the full range of atmospheric conditions (i.e., oxidizing and reducing conditions) prevalent in the various experiments. The release behavior of the low-volatile species are controlled by the rate-limiting step of fission-product vaporization from the fuel surface (F_v). On the other hand, the release behavior of xenon and the other more-volatile species (typically, cesium, iodine, antimony and tellurium) are determined by the slower matrix diffusion step (F_d). The release fractions for the various release mechanisms were evaluated at each time step of ~ 1 min, in which the corresponding rate-limiting step was determined [38]. For some isotopes, the overall release fraction (F) in Table 9 is smaller than that given for either diffusion (F_d) or vaporization (F_v). This result arises when there is an insufficient diffusional release (or matrix-stripping release) to keep up with the fission-product vaporization from the fuel surface early in the experiment. The results in Table 9 also show that releases of the relatively-volatile tellurium and antimony species are somewhat restricted due to chemical trapping in the Zircaloy cladding (see Section 2.3).

The measured release fractions of ^{144}Ce and ^{106}Ru have been inferred from the release behavior of their short-lived daughter products (^{144}Pr and ^{106}Ru). Due to the very short half-life of 29.8 s for ^{106}Ru, the measured release fraction of this isotope is directly indicative of the parent fraction (see Appendix A). No significant release of ^{144}Pr (half-life of 17.3 min) was observed within the measurement uncertainty up to the end of the high-temperature steam period in Fig. 6(c). Consequently, it is believed that the cumulative release of this isotope is attributable solely to the release of its parent (which would therefore affect the parent–daughter equilibrium in accordance with Appendix A). However, if some release of ^{144}Pr did in fact occur, the stated value in Table 9 would be an overestimate of the measured release of ^{144}Ce (i.e., some release of ^{144}Pr is expected on thermodynamic grounds as a consequence of a finite partial pressure for this species). In this case, the model prediction would be in better agreement with experiment.

The underprediction of the cesium release fraction in Vercors-2 (resulting from the rate-controlling vaporization process) suggests that an important volatile compound

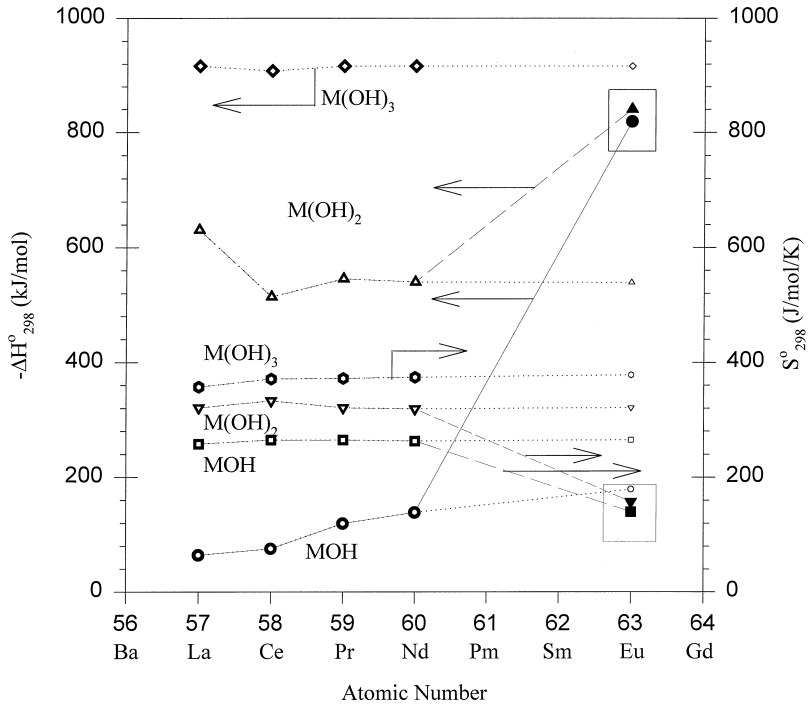

Fig. 8. Enthalpy change and absolute entropy plotted against atomic number for the lanthanide hydroxides. The larger symbols for Eu correspond to the data in the Victoria code. The smaller symbols for Eu are extrapolated values from the given trends of the lanthanide series (as used in the present analysis).

(such as cesium telluride) may have been omitted in the present thermodynamic analysis (see Table 3). In particular, this suggestion is supported by the fact that the predicted diffusion release fraction (F_d) is in good agreement with experiment. In the previous analysis of Ref. [4], the vaporization process was not considered for the cesium release prediction. In addition, the europium release is overestimated in all cases, which is particularly significant where a hydroxide compound predominates (Table 10). In fact, the original thermodynamic data of Ref. [21] yielded an unrealistically high vapor pressure for the europium hydroxide compounds, EuOH and $Eu(OH)_2$. As shown in Fig. 8, the thermodynamic data from the Victoria code [21] for these compounds are not consistent with the enthalpy change and absolute entropy data for the hydroxides of the other lanthanide series elements taken from Cubicciotti [6]. Instead, a new set of thermodynamic quantities were estimated for the europium hydroxides (see Table 3) for use in the present FACT analysis, based on an extrapolation of the trends in the data presented in Fig. 8. However, this extrapolated set still results in an overprediction of the partial pressure for europium, as shown in Table 9, indicating a need for better thermochemical data for the hydroxide forms of europium.

In the present analysis, all 'low-volatile' fission products are treated equivalently ignoring the effects of their solubility in the UO_2 lattice, i.e., Zr and the rare earths (e.g., Ce, Pr, Nd, and Eu) are soluble in the fuel matrix whereas Mo, Ru and probably Ba at higher burnup are not [40]. Consequently, the soluble fission products can have a non-zero boundary condition at the end of their diffusion path (which depends on the rate of the gas-phase mass transfer step). This situation is contrary to that assumed in the derivation of the Booth diffusion model of Eq. (2). The present treatment will therefore yield a conservative estimate of the diffusion release fraction (F_d) for these species. However, if the rate-controlling step is indeed vaporization (e.g., see Table 9), this result will not have a significant effect on the overall release fraction in accordance with Eq. (27). On the other hand, the insoluble fission products always have a zero concentration in the lattice adjacent to a free surface or grain boundary where, for instance, metallic inclusions will result. In this case, the condition given by Eq. (27) applies.

As expected in a reducing hydrogen atmosphere, or in a hydrogen/steam gas mixture, as prevalent in the CEA zircaloy-clad tests, the amount of fuel volatilization (i.e., F_{vol}) is small due to the presence of a lower UO_3 partial pressure (see Table 9). Hence, matrix stripping is not an important fission-product release process in this case. On the other hand, in the CRL fuel-fragment test conducted in steam (MCE2-T19), significant fuel volatilization occurred. In fact, the fuel volatilization fraction predicted with the thermodynamic/mass transfer model of Section 2.2 (i.e., $F_{vol} = 70\%$ in Table 9) was in excellent agreement with observation, as inferred from the measured pre- and post-test sample masses in Table 7, i.e., $\Delta m/m = (0.200 - 0.046\ \text{g})/(0.200\ \text{g}) \sim 77\%$.

3.3.1. Comparison of fuel volatilization models

The fuel volatilization model of Section 2.2 can also be compared to that developed by Alexander and Ogden [9]. In the derivation of the latter model, it is implicitly assumed that the sublimation rate per unit area (Z) can be described by an effusion process in accordance with the Knudsen equation [41],

$$Z = \frac{p}{(s\pi mkT)^{1/2}}, \tag{44}$$

where p and T are the pressure and temperature of the gas, m is the molecular mass and k is Boltzmann's constant. The mass loss rate expression, as employed in Ref. [9], therefore follows where [41]

$$\dot{m}_0 = mZ = p\left(\frac{m}{2\pi kT}\right)^{1/2} = 44.3\,p\left(\frac{M}{T}\right)^{1/2}. \tag{45}$$

For the last expression of Eq. (45), $\dot{m}_0$ is given in units of g cm^{-2} s^{-1}, where M is the molar mass (g mol^{-1}), p is in bar and T is in K [9]. The overall vaporization mass flux (dm/dt) (in g cm^{-2} s^{-1}) then follows by accounting for the subsequent mass transport across a film boundary layer. Hence, using a heat/mass transfer analogy based on a Langmuir analysis for the flow of heat from a cylindrical wire of radius a across a film boundary layer of thickness b [9],

$$\frac{dm}{dt} = \dot{m}_0\left\{\frac{c_1}{\ln(b/a)}\frac{T^{1.75}}{p_{tot}^{2/3}}\sqrt{1 + 0.05U_\infty}\right\}, \tag{46}$$

where $c_1 = 1.16 \times 10^{-8}$, $\ln(b/a) = 0.331$, T is in K, p_{tot} is in bar and U_∞ is the bulk stream velocity in cm s^{-1}. The fuel volatilization model of Eqs. (45) and (46) has been adopted for both the Victoria and ELSA computer codes [21,42], in which the partial pressure p for UO_3 resulting from an average UO_{2+x} composition is evaluated from

$$p_{UO_3} = p_{O_2}^{0.45}\exp\left\{-\frac{\Delta G_{(UO_3)}}{RT}\right\}, \tag{47}$$

where $\Delta G_{(UO_3)} = 59\,700 - 19.9T$ (cal mol^{-1}). Inspection of Eqs. (14) and (47) shows that the average stoichiometry deviation is arbitrarily set to $x = 0.1$ in Eq. (47). The term in curly brackets in Eq. (46) is also set to a representative value of 20% in the Victoria code, based on the specific experimental results of Alexander and Ogden. On comparison of the two models, it can be seen that the temperature and pressure dependencies are quite different, i.e., Eqs. (45) and (46) predict dependencies of $T^{1.25}$ and $p_{tot}^{-2/3}$ whereas Eqs. (18), (28) and (29) predict dependencies of $T^{1/2}$ and p_{tot}^{-1}. Moreover, for the present analysis, the model of Alexander and Ogden predicts a much greater vaporization by a factor of ~ 70. A similar observation was made by Manenc and Notley who subsequently ad-

justed the fitted coefficient in Eq. (46) to other experimental data for the implementation of the model into the ELSA code [42]. However, it is important to note that Eq. (45) is only strictly applicable to an effusion process. In this type of process, gas at a uniform pressure, p, is typically allowed to escape into a vacuum through a very small hole in a container and, hence, is unable to return into the container. This situation is not strictly applicable to the percolation of UO_3 vapor in the inter-connected tunnels and at the surface of the fuel specimen in which the gas concentration is no longer uniform but where, in fact, a concentration gradient exists. In reality, UO_3 molecules that travel in one direction are also free to return to their initial region where bulk migration results from a net flux.

Thus, the use of the Alexander and Ogden model for the calculation of fuel volatilization is questionable as a result of the assumption of effusive flow. On the other hand, the present model of Section 2.2 is self consistent with the given formalism for fission product vaporization (Section 2.3), and is in excellent agreement with the CRL test results (Section 3.3). In addition, contrary to the Alexander and Ogden model, no adjustable constants have been used in the present treatment, i.e., this model is based on thermochemical data and a well-established heat (mass) transfer coefficient for annular flow.

4. Conclusions

(1) A model has been developed to describe the release behavior of low-volatile fission products from uranium dioxide fuel during severe reactor accident conditions. The vaporization model is based on the equilibrium partial pressures of the fission products and mass transport theory. The equilibrium partial pressures were determined by Gibbs-energy minimization with the FACT thermodynamics package for a system consisting of a condensed phase (UO_2 plus fission products) and a gas phase (H_2O and H_2 plus gaseous fission products). The extensive FACT results were recast into an analytical form, using the method of chemical potentials, for model implementation into a stand-alone computer code.

(2) A theoretical treatment has also been used to describe the effect of fuel volatilization on the fission-product release behavior. The model includes the effects of the fuel oxidation kinetics on the production of UO_3 vapor and the subsequent mass transfer of this gaseous phase through a boundary layer at the surface of the fuel. This matrix-stripping process competes with that of solid-state diffusion as a mechanism of fission-product release to the fuel surface.

(3) The model is in good agreement with the fission-product release data obtained in the CEA tests, Heva-6 and Vercors-2, which were conducted with zircaloy-clad fuel specimens at temperatures of 2370 and 2100 K, in a hydrogen and steam atmosphere, respectively. The model has also been validated against fission-product release data from the CRL test, MCE2-T19, performed with a fuel-fragment specimen at 2300 K in steam. This model is also able to predict the observed fuel volatilization in the CRL test.

Acknowledgements

The present analysis was supported by the Natural Sciences and Engineering Research Council of Canada (award No. OGP0155726). The CRL experiment was supported by Atomic Energy of Canada Limited, Ontario Hydro, Hydro Quebec and New Brunswick Electric Power Corporation under the Candu Owners Goup agreement. The CEA experiments were supported by both the Institut de Protection et de Sûreté Nucléaire and the Electricité de France. The authors would like to thank B. André, G. Ducros and M. Tourasse (Centre d'Etudes Nucléaires de Grenoble) for many helpful discussions on the Heva-Vercors program, and D.R. Olander (University of California, Berkeley) for a review of the paper. Finally, the authors wish to recognize the pioneering work on Gibbs-energy minimization for fission-product vaporization by the late D. Cubicciotti of the Electric Power Research Institute.

Appendix A. Calculation of release fraction for parent–daughter pair

The mass balance equations for the rate of change of the inventory of a given parent (1)-daughter (2) fission-product pair contained in an irradiated fuel sample are

$$\frac{\mathrm{d}N_1}{\mathrm{d}t} = -R_1(t) - \lambda_1 N_1, \tag{A.1}$$

$$\frac{\mathrm{d}N_2}{\mathrm{d}t} = -R_2(t) - \lambda_2 N_2 + \lambda_1 N_1, \tag{A.2}$$

where R is the release rate due to fission-product vaporization from the sample and λ is the radioactive decay constant. At the start of the annealing experiment, it is assumed that $N_1(t=0) = N_{10}$ and $N_2(t=0) = N_{20}$.

The solution of Eqs. (A.1) and (A.2), subject to the given initial conditions, is

$$N_1(t) = N_{10}\,\mathrm{e}^{-\lambda_1 t} - \mathrm{e}^{-\lambda_1 t}\int_0^t R_1(\tau)\mathrm{e}^{\lambda_1 \tau}\,\mathrm{d}\tau, \tag{A.3}$$

$$N_2(t) = N_{20}\,\mathrm{e}^{-\lambda_2 t} + \frac{\lambda_1 N_{10}}{\lambda_2 - \lambda_1}\left[\mathrm{e}^{-\lambda_1 t} - \mathrm{e}^{-\lambda_2 t}\right] - \mathrm{e}^{-\lambda_2 t}\left\{\int_0^t R_2(\tau)\mathrm{e}^{\lambda_2 \tau}\,\mathrm{d}\tau + \lambda_1\int_0^t \mathrm{e}^{(\lambda_2-\lambda_1)\tau} \times\left[\int_0^\tau R_1(\xi)\mathrm{e}^{\lambda_1 \xi}\,\mathrm{d}\xi\right]\mathrm{d}\tau\right\}. \tag{A.4}$$

In the Chalk River experiment, the release fraction was obtained from a direct measurement of the activity (A) by following a gamma-ray of a particular isotope, such that

$$F = \frac{A_{20} - A_2(t)}{A_{20}} = \frac{\lambda_2 N_{20} - \lambda_2 N_2(t)}{\lambda_2 N_{20}}. \quad (A.5)$$

Substituting Eq. (A.4) into the second relation of Eq. (A.5) yields

$$F(t) = (1 - e^{-\lambda_1 t}) + e^{-\lambda_2 t}\left\{\int_0^t \frac{R_2(\tau)}{N_{20}} e^{\lambda_2 \tau}\, d\tau + \lambda_2 \int_0^t e^{(\lambda_2 - \lambda_1)\tau}\left[\int_0^\tau \frac{R_1(\xi)}{N_{10}} e^{\lambda_1 \xi}\, d\xi\right] d\tau\right\}. \quad (A.6)$$

In the derivation of Eq. (A.6) it has been assumed that the parent isotope has a very long half-life compared to that of the daughter isotope so that an equilibrium is established after the initial irradiation period; thus, an equilibrium exists prior to the anneal where $\lambda_1 N_{10} = \lambda_2 N_{20}$.

If the release rate of the parent and daughter isotopes are constant in time, and $\lambda_2 \gg \lambda_1$, Eq. (A.6) reduces further to

$$F = (1 - e^{-\lambda_1 t}) + \frac{R_2 t}{N_{20}}\left[\frac{1 - e^{-\lambda_2 t}}{\lambda_2 t}\right] + \frac{R_1 t}{N_{10}} \approx F_2\left[\frac{1 - e^{-\lambda_2 t}}{\lambda_2 t}\right] + F_1. \quad (A.7)$$

In the second relation, the release fractions for the parent and daughter isotopes are defined, respectively, as $F_1 = R_1 t/N_{10}$ and $F_2 = R_2 t/N_{20}$. Interestingly, if the daughter isotope has a very short half-life, were $\lambda_2 t \gg 1$, then the observed release fraction (as obtained by the monitoring of the gamma ray of the daughter isotope) is simply due to that of the parent, i.e., $F \approx F_1$. In fact, this situation corresponds to the measurement of ^{106}Ru in Table 9 where the measured gamma-ray of the short-lived isotope ^{106}Rh (half-life of 29.8 s) simply reflects the release behavior of its long-lived parent ^{106}Ru (half-life of 372.6 d).

References

[1] M.F. Osborne, R.A. Lorenz, Nucl. Safety 33 (1992) 344.
[2] B.J. Lewis, B. Andre, B. Morel, P. Dehaudt, D. Maro, P.L. Purdy, D.S. Cox, F.C. Iglesias, M.F. Osborne, R.A. Lorenz, J. Nucl. Mater. 227 (1995) 83.
[3] A.B. Reynolds, J.L. Kelly, S.T. Kim, Nucl. Technol. 74 (1986) 76.
[4] B.J. Lewis, B. Andre, G. Ducros, D. Maro, Nucl. Technol. 116 (1996) 34.
[5] D. Cubicciotti, in: Advances in Ceramics, vol. 17, American Ceramic Society, Columbus, OH, 1986, p. 211.
[6] D. Cubicciotti, J. Nucl. Mater. 154 (1988) 53.
[7] D. Cubicciotti, B.R. Sehgal, Nucl. Technol. 65 (1984) 267.
[8] C.A. Alexander, J.S. Ogden, L. Chan, R.W. Wright, Matrix stripping and fission product release at high temperatures, Proc. Int. Symp. on Severe Accidents in Nuclear Power Plants, Sorrento, Italy, Mar. 21–25, 1988, IAEA-SM-296/99, International Atomic Energy Agency, 1988.
[9] C.A. Alexander, J.S. Ogden, High Temp. High Pressures 21 (1990) 149.
[10] D.S. Cox, C.E.L. Hunt, Z. Liu, F.C. Iglesias, N.A. Keller, R.D. Barrand, R.F. O'Connor, A model for the release of low-volatility fission products in oxidizing conditions, Proc. 12th Annual Conf. of the Canadian Nuclear Society, Saskatoon, Saskatchewan, Canada, June 9–12, 1991, AECL-10440, Atomic Energy of Canada Ltd.
[11] C.W. Bale, A.D. Pelton, W.T. Thompson, Facility for the Analysis of the Chemical Thermodynamics, McGill University and École Polytechnique, 1995.
[12] D.R. Stull, H. Prophet, JANAF Thermochemical Tables, 2nd ed., National Standard Reference Data System, NSRDS-NBS 37, US Department of Commerce, National Bureau of Standards, Washington, DC, June, 1971 (and updates).
[13] I. Barin, O. Knacke, Thermochemical Properties of Inorganic Substances, Springer, Berlin, 1973.
[14] I. Barin, O. Knacke, O. Kubaschewski, Thermochemical Properties of Inorganic Substances, Supplement, Springer, Berlin, 1977.
[15] E.H.P. Cordfunke, R.J.M. Konings, Thermochemical Data for Reactor Materials and Fission Products, North Holland, Elsevier Science, Amsterdam, 1990.
[16] F. Garisto, Thermodynamic Behavior of Ruthenium at High Temperatures, Atomic Energy of Canada Ltd., AECL-9552, 1988.
[17] T.B. Lindemer, T.M. Besmann, C.E. Johnson, J. Nucl. Mater. 100 (1981) 178.
[18] S. Dash, Z. Singh, R. Prasad, D.D. Sood, J. Nucl. Mater. 207 (1993) 350.
[19] R. Saha, R. Babu, K. Nagarajan, C.K. Mathews, J. Nucl. Mater. 167 (1989) 271.
[20] H. Kleykamp, J. Nucl. Mater. 167 (1989) 49.
[21] T.J. Heames, D.A. Williams, N.E. Bixler, A.J. Grimley, C.J. Wheatley, N.A. Johns, P. Domagala, L.W. Dickson, C.A. Alexander, I. Osborn-Lee, S. Zawadzki, J. Rest, A. Mason, R.Y. Lee, VICTORIA: A Mechanistic Model of Radionuclide Behavior in the Reactor Coolant System Under Severe Accident Conditions, US Nuclear Regulatory Commission, NUREG/CR-5545, SAND90-0756, Rev. 1, R3, R4, December 1992.
[22] B. Andre, G. Ducros, J.P. Leveque, D. Maro, M.F. Osborne, R.A. Lorenz, Nucl. Technol. 114 (1996) 23.
[23] P. Purdy, Master of Science (Engineering) dissertation, Department of Physics, Queen's University, 1995.
[24] F. Capone, J.P. Hiernaut, M. Martellenghi, C. Ronchi, Nucl. Sci. Eng. 124 (1996) 436.
[25] P.E. Blackburn, J. Nucl. Mater. 46 (1973) 244.
[26] D.S. Cox, R.F. O'Connor, W.W. Smeltzer, Solid-State Ionics 53–56 (1992) 238.
[27] A.C. Brito, F.C. Iglesias, Y. Liu, C.J. Westbye, D.S. Cox, B.J. Lewis, Modelling of UO_2 oxidation in steam, Proc. 17th Annual Conf. of the Canadian Nuclear Society, Fredericton, New Brunswick, Canada, June 9–12, 1996, C.2, Canadian Nuclear Society, 1996.

[28] O. Kubaschewski, C.B. Alcock, Metallurgical Thermochemistry, 5th ed., Pergamon, New York, 1979.
[29] R.J. Ackermann, A.T. Chang, J. Chem. Thermodyn. 5 (1973) 873.
[30] D.S. Cox, FOXSIM Version 2: Fuel oxidation simulation for UO_2 in air and steam, Atomic Energy of Canada Limited, Internal Report RC-402, February 1990.
[31] R.B. Bird, W.E. Stewart, E.N. Lightfoot, Transport Phenomena, Wiley, New York, 1960.
[32] G. Le Bas, The Molecular Volumes of Liquid Chemical Compounds, Longmans, Green, London, 1915.
[33] R.H. Perry, C.H. Chilton, Chemical Engineers' Handbook, 5th ed., McGraw-Hill, New York, 1973, pp. 3–229.
[34] R.C. Reid, J.M. Prausnitz, B.E. Poling, The Properties of Gases and Liquids, 4th ed., McGraw-Hill, New York, 1987.
[35] B.J. Lewis, W.T. Thompson, M.H. Kaye, B.J. Corse, F.C. Iglesias, B. André, G. Ducros, M. Tourasse, D. Maro, Vaporization of low-volatile fission products in severe light water reactor accidents, Proc. Int. Topical Meeting on Light Water Reactor Fuel Performance, Portland, OR, Mar. 2–6, 1997.
[36] M.H. Kaye, B.J. Lewis, W.T. Thompson, F.C. Iglesias, Oxidation of nuclear fuel rods during a loss-of-coolant accident, 8th Canadian Materials Science Conference, London, Ontario, June 11–14, 1996.
[37] M.R. Spiegel, Mathematical Handbook of Formulas and Tables, Schaum's Outline Series, McGraw-Hill, New York, 1968, p. 147.
[38] B. Corse, Master of Engineering dissertation, Department of Chemistry and Chemical Engineering, Royal Military College of Canada, 1997.
[39] M.I. Mendelson, J. Am. Ceram. Soc. 52 (1969) 443.
[40] S.G. Prussin, D.R. Olander, W.K. Lau, L. Hansson, J. Nucl. Mater. 154 (1988) 25.
[41] P. Atkins, Physical Chemistry, 5th ed., Freeman, New York, 1994.
[42] H. Manenc, M.J. Notley, ELSA: A simplified code for fission product release calculations, Transactions of the American Nuclear Society, 1996 International Conference on the Global Benefits of Nuclear Technology, November 10–14, 1996, Washington, DC, vol. 75, TANSAO 75 1-490, 1996, ISSN 0003-018X, p. 250, American Nuclear Society, La Grange Park, IL, 1996.